© 2017. Published by The Company of Biologists Ltd | Development (2017) 144, 95-105 doi:10.1242/dev.139865

RESEARCH ARTICLE

# Remodeling of adhesion and modulation of mechanical tensile forces during apoptosis in *Drosophila* epithelium

**Xiang Teng[1,2], Lei Qin[2], Roland Le Borgne[3,4] and Yusuke Toyama[1,2,5,*]**

## ABSTRACT

Apoptosis is a mechanism of eliminating damaged or unnecessary cells during development and tissue homeostasis. During apoptosis within a tissue, the adhesions between dying and neighboring non-dying cells need to be remodeled so that the apoptotic cell is expelled. In parallel, contraction of actomyosin cables formed in apoptotic and neighboring cells drives cell extrusion. To date, the coordination between the dynamics of cell adhesion and the progressive changes in tissue tension around an apoptotic cell is not fully understood. Live imaging of histoblast expansion, which is a coordinated tissue replacement process during *Drosophila* metamorphosis, shows remodeling of adherens junctions (AJs) between apoptotic and non-dying cells, with a reduction in the levels of AJ components, including E-cadherin. Concurrently, surrounding tissue tension is transiently released. Contraction of a supra-cellular actomyosin cable, which forms in neighboring cells, brings neighboring cells together and further reshapes tissue tension toward the completion of extrusion. We propose a model in which modulation of tissue tension represents a mechanism of apoptotic cell extrusion.

**KEY WORDS: Apoptosis, Cell adhesion, *Drosophila*, Force, Tissue mechanics**

## INTRODUCTION

Throughout development and adult life, epithelia undergo constant growth and turnover. As a cell population changes, epithelial architecture needs to be maintained and this is achieved through tight intercellular adhesions supported by adherens junctions (AJs) (Harris and Tepass, 2010; Takeichi, 2014; Lecuit and Yap, 2015). Apoptosis, or programmed cell death, is the most common mechanism of eliminating damaged or unnecessary cells during embryonic development and tissue homeostasis (Jacobson et al., 1997). When cells within a tissue undergo apoptosis, the adhesions between the dying and neighboring non-dying cells need to be remodeled. This ensures the apoptotic cell can be expelled from a tissue without compromising tissue cohesion. Loss of adhesions in the apoptotic process has been studied, with a focus on the disruption of cell-cell junctions associated with caspase activation. Members of the caspase family serve as the key executors of apoptosis (Riedl and Shi, 2004; Miura, 2012). For instance, AJ components, such as E-cadherin (Shotgun, E-cad) and β-catenin (β-cat) are known substrates of caspase 3 in mammalian cells (Bannerman et al., 1998; Brancolini et al., 1997). In *Drosophila*, a reduction in the levels of E-cad from AJs is associated with cleavage of the β-cat homolog Armadillo by the *Drosophila* effector caspase DrICE (Kessler and Muller, 2009).

Along with AJ remodeling, the process of cell extrusion is also crucial in the expulsion of dying cells from a tissue. In tissue culture, apoptotic cells autonomously develop an actomyosin cable, and the neighboring non-apoptotic cells also form a supra-cellular actomyosin purse-string (Rosenblatt et al., 2001; Kuipers et al., 2014). These cables exert contractile force and contribute to extrusion (Rosenblatt et al., 2001; Kuipers et al., 2014). Recently, it was shown that E-cad is crucial for the transmission of contractile force to neighboring cells (Lubkov and Bar-Sagi, 2014), and for the recruitment of coronin 1B, which aligns the actomyosin cable (Michael et al., 2016) during apoptotic cell extrusion. Together, these findings highlight an intriguing interplay between AJ dynamics and the cytoskeleton, which leads to progressive changes in tissue tension around the apoptotic cell. The mechanisms resulting from this interplay remain to be fully understood.

We elected to study tissue replacement during histoblast expansion in *Drosophila*. At the onset of pupal development, the quiescent abdominal histoblasts (precursors of the adult epidermal cells) are grouped in nests embedded amongst larval epidermal cells (LECs) (Fig. 1A; Movie 1). As metamorphosis progresses, histoblasts exhibit rapid proliferation and active migration, leading to growth and expansion of the nests (Ninov et al., 2007, 2010). Concurrently, pre-existing LECs undergo caspase-3-mediated apoptosis (Nakajima et al., 2011). The majority of the apoptotic cells in *Drosophila*, including LECs, extrude basally. This is observed in, for example, embryonic tissue (Kiehart et al., 2000; Toyama et al., 2008; Meghana et al., 2011; Muliyil et al., 2011; Sokolow et al., 2012; Monier et al., 2015), larval tissue (Ninov et al., 2007), imaginal discs (Shen and Dahmann, 2005; Manjón et al., 2007; Monier et al., 2015) and adult tissue during pupa (Kuranaga et al., 2011; Marinari et al., 2012). Intriguingly, this is in contrast to apical cell extrusion in most vertebrates (Rosenblatt et al., 2001; Eisenhoffer et al., 2012; Yamaguchi et al., 2011). Around 80% of LECs undergo apoptosis in proximity to histoblast nests (hereafter referred to as 'boundary' LECs) and ∼20% of LECs die away from the nests (hereafter referred to as 'non-boundary' LECs) (Ninov et al., 2007; Bischoff and Cseresnyes, 2009; Nakajima et al., 2011). Although proliferation of histoblasts is known to contribute to histoblast expansion (Ninov et al., 2007; Ninov et al., 2010), it was not clear whether the mechanics of LEC apoptosis also contributes to the expansion (Ninov et al., 2007; Bischoff and Cseresnyes, 2009).

In this study, we reveal that during the extrusion of apoptotic LECs, AJs between apoptotic and neighboring cells become remodeled, and that this is associated with a reduction in the levels of AJ components. Furthermore, this correlates with a transient release of tissue tension. Towards the end of the extrusion process, neighboring cells are

[1]Department of Biological Sciences, National University of Singapore, Singapore 117543. [2]Mechanobiology Institute, National University of Singapore, Singapore 117411. [3]CNRS, UMR 6290, Institute of Genetics and Development of Rennes, F-35043 Rennes, France. [4]Université Rennes 1, Faculté de Médecine, F35043 Rennes, France. [5]Temasek Life Sciences Laboratory, Singapore 117604.

*Author for correspondence (dbsty@nus.edu.sg).

Y.T., 0000-0003-3230-1062

**Received 18 May 2016; Accepted 10 November 2016**

Development (2017) 144, 95-105 doi:10.1242/dev.139865

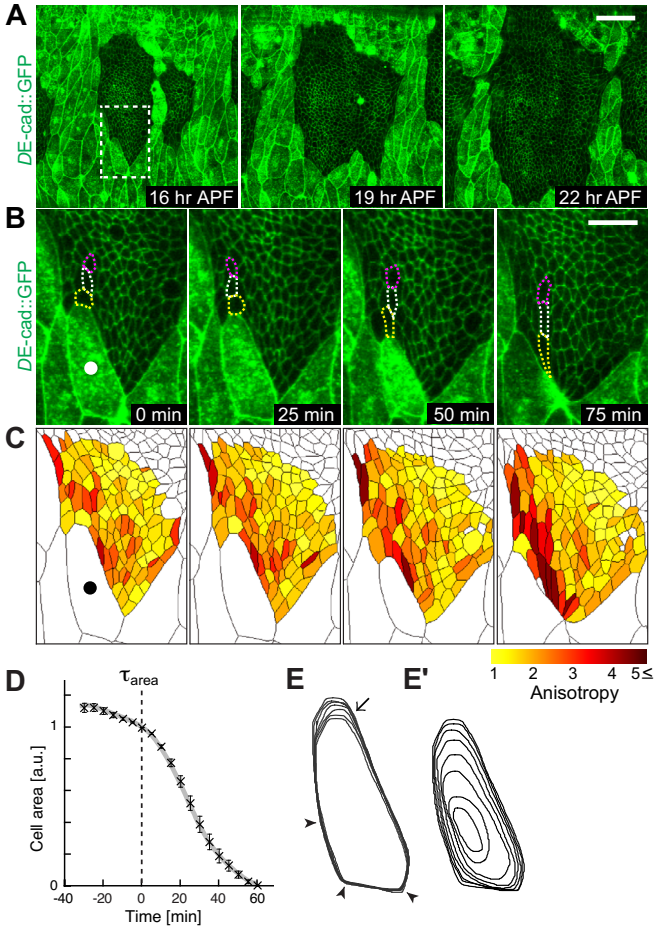


**Fig. 1. Kinematics of apoptotic LECs and surrounding histoblast cells during histoblast expansion.** (A) Confocal images of a wild-type pupa expressing *D*E-cad::GFP, showing anterior and posterior dorsal histoblast nests and larval epithelial cells (LECs) at 16, 19 and 22 h after puparium formation (APF) (Movie 1). (B) High magnification of the boxed region in A (Movie 2). Imaging started at 0 min. An apoptotic LEC (filled circle), the nearest-neighbor cell (yellow dotted line), and the cells that are not directly attached to the apoptotic LEC (white and magenta dotted lines) are highlighted. Anterior is to the left and ventral to the top in all figures. (C) Color-coded reproduction of the confocal images shown in B (Movie 4). Colors denote the anisotropy of cell shape. The darker colors represent more elongated cells. (D) Graph plotting the normalized apical cell area of apoptotic cells over time ($n$=21). $\tau_{area}$ (dashed line) denotes the time when the cell started to constrict with higher speed. Error bars indicate s.e.m. (E) Contour plots showing the deformation in the shape of the apoptotic cell highlighted in B prior to $\tau_{area}$. Cell deformation is local, as highlighted by the arrow. Arrowheads highlight the cell boundary with little deformation. (E′) Contour plots of the apoptotic cell from $\tau_{area}$ onwards. Scale bars: 50 µm (A); 20 µm (B).

brought together by the formation and contraction of supra-cellular actomyosin cables within the neighboring cells. This further restores tissue tension. We conclude that adhesion remodeling and changes in tissue tension are mechanically coordinated, and that this represents a mechanism of apoptotic cell extrusion. Furthermore, we reveal that the extrusion process of death-committed LECs is able to drive histoblast expansion mechanically.

## RESULTS

### Apoptotic cell extrusion coincides with neighboring cell deformation

To explore the effects of extrusion of apoptotic LECs on histoblast expansion, we collected confocal images of the surface of wild-type pupae expressing a *D*E-cad::GFP (*Drosophila* E-cadherin GFP). We found that boundary LECs undergo apical constriction (Fig. 1B, filled circle; Movie 2) and basal extrusion (Movie 3). Concurrently, histoblast cells surrounding apoptotic LECs exhibited biased cell shape deformations (Fig. 1B). Histoblasts that directly contact apoptotic LECs become progressively elongated (Fig. 1B, yellow dotted outlines). The next-to-nearest-neighbor histoblasts also elongated (Fig. 1B, white and magenta dotted outlines). With time, the space originally occupied by the apoptotic LECs was covered by neighboring cells. To quantify histoblast deformation upon boundary LEC extrusion, we monitored cell elongation by measuring the anisotropy of cell shape (Materials and Methods; Fig. 1C; Movie 4). Analyzing the anisotropy revealed that histoblast elongation correlated with LEC extrusion (Fig. 1C), and the degree of elongation decayed as a function of the distance from the extruding cell (Fig. S1A). These observations indicated that the mechanical impact of apoptotic cell extrusion was not restricted to the nearest-neighbor histoblast, but propagated to the next-to-nearest-neighbor cells. The elongated histoblasts (Fig. 1B) underwent either cell division or cell-cell junction remodeling after cell extrusion had completed, and did not maintain their elongated shape (Fig. S2). These rearrangements, however, had no impact on tissue expansion, with the edge of the histoblasts remaining in place after cell extrusion was complete (Fig. S2). This suggests that the mechanical impact of boundary LEC apoptosis on tissue expansion is preserved even after the completion of LEC extrusion.

To examine the kinematics of extruding LECs further, we analyzed the temporal progression of cell shape changes. Boundary LECs exhibited an apical constriction in the course of cell extrusion (Fig. 1D). The time at which the cell area transitioned, $\tau_{area}$, was defined as the time when the cell started to constrict with higher speed (Materials and Methods; Fig. S3). Intriguingly, the boundary LECs exhibited characteristic kinematics before and after $\tau_{area}$. The deformation in the shape of an extruding LEC was local and anisotropic before $\tau_{area}$. Here, the major deformation was at the cell boundary adjacent to the growing histoblasts (Fig. 1E, arrow), whereas the cell boundaries next to adjacent LECs showed little or no deformation (Fig. 1E, arrowheads). We speculate that the local deformation, before $\tau_{area}$, was due to compressive stress exerted by proliferating histoblasts, which caused LECs to be passively deformed. By contrast, the contraction of the dying LEC was more isotropic after $\tau_{area}$ (Fig. 1E′), which might have been due to the contraction of actomyosin rings formed upon apoptosis. The different kinematics of apoptotic LECs before and after $\tau_{area}$ were further supported by quantitative measurements of the cell shape (Fig. S4). Moreover, quantification of a non-extruding LEC that was next to an LEC undergoing extrusion revealed that although it was static before $\tau_{area}$, it exhibited local deformations in response to the extrusion of its neighboring cell (Fig. S5A). In this case, the major deformation after $\tau_{area}$ was at the cell boundary adjacent to the extruding LEC. The cell boundaries away from the cell undergoing extrusion showed little or no deformation (Fig. S5B,B′). Together, we found that the effect of boundary LEC extrusion was restricted to the nearest-neighbor LECs, but propagated into several layers of histoblasts.

We also noticed that apoptosis of non-boundary LECs was not strongly associated with histoblast deformation (Fig. S6). Hereafter, we focus on the apoptotic process of boundary LECs, which contributes mechanically to histoblast expansion.

### Caspase-3 activation precedes apical constriction in apoptotic cells

To clarify the time at which apical constriction commenced, with respect to apoptotic signaling, we monitored caspase activity in

Development (2017) 144, 95-105 doi:10.1242/dev.139865

LECs by imaging pupae incorporating a genetically encoded fluorescence resonance energy transfer (FRET)-based caspase-3-like DEVDase (hereafter referred to as caspase-3) sensor (SCAT3) (Takemoto et al., 2003; Nakajima et al., 2011; Levayer et al., 2016). This sensor displayed a reduced FRET ratio as caspase-3 activation increased (Fig. 2A; Materials and Methods). We used the bipartite GAL4-UAS system (Brand and Perrimon, 1993) to express SCAT3 in the pupal epithelium, including LECs, by *tsh*-GAL4. To monitor the apical constriction of apoptotic LECs in parallel with caspase-3 activity, we imaged *D*E-cad::Tomato$^{KI}$ (Huang et al., 2009) together with SCAT3 (Fig. 2B). Caspase-3 activity progressively increased with time (Fig. 2A; Movie 5; Fig. 2C, orange line). The initiation of caspase-3 activation was defined as $\tau_{Cas3}$, the time when the cell started to show higher caspase-3 activity (Fig. S3). The time delay between $\tau_{area}$ and $\tau_{Cas3}$ indicated that the initiation of caspase-3 activation preceded the onset of apical constriction (Fig. 2D). Qualitatively, our data are in an agreement with recent findings from apoptotic extrusion in *Drosophila* notum (Levayer et al., 2016).

### Remodeling of AJs during apoptotic cell extrusion

To understand how AJs and the associated cytoskeleton were remodeled in the course of LEC apoptosis, we examined the distribution of E-cad (*ubi-D*E-cad::GFP) and Myosin II [non-muscle Myosin II regulatory light chain (Spaghetti squash, Sqh); MyoII::mCherry]. Stills from time-lapse movies show that the level of E-cad at the interfaces between apoptotic LECs and neighboring cells, including both histoblasts and non-apoptotic LECs, was reduced (Fig. 3A,A′, arrowheads; Movie 6). By contrast, there was no change in the level of *D*E-cad::GFP at cell junctions of neighboring cells, away from the interface (Fig. 3A′, double arrows). Concomitant to the reduction of E-Cad, MyoII distribution around the periphery of apoptotic LECs showed two myosin cable-like structures (Fig. 3B, arrows and double arrows). Merged images of E-cad and MyoII (Fig. 3C) indicated that the supra-cellular cable was in the neighboring cells (referred to as the 'outer' cable; Fig. 3B,D, double arrows) whereas the other cable was in the apoptotic cell (referred to as the 'inner' cable; Fig. 3B,D, arrows). The distribution of actin resembled that of MyoII (Fig. S7). We also noticed that E-cad accumulated between the two neighboring cells (Fig. 3C′, arrows). These loci could link the actomyosin cables, thereby forming a supra-cellular actomyosin purse-string-like structure. Importantly, upon completion of apical constriction, *de novo* AJs were formed between the non-apoptotic neighboring cells (Fig. 3A, t=45 min; Fig. S8).

To characterize further the progressive reduction of E-cad levels at the interfaces between apoptotic LECs and their neighboring cells, we imaged a GFP knock-in fly line that replaced the endogenous *D*E-cad (*D*E-cad::GFP$^{KI}$) (Huang et al., 2009). The level of E-cad at the interface between apoptotic LECs and neighboring cells progressively decreased with time (Fig. 3E) and the initiation of the decrease in the level of E-cad ($\tau_{EcadKI}$) followed the onset of apical constriction ($\tau_{area}$) (Fig. 3E,F). Furthermore, we found that E-cad levels in pupae with two copies of E-cad [E-cad::GFP$^{KI}$; $\tau_{EcadKI\_red}$ 38.3±3.4 min (mean±s.e.m.) after $\tau_{area}$, $n$=6; Fig. 3F] or with four copies of E-cad (*ubi*-E-cad::GFP; $\tau_{Ecad\_red}$ 36.4 ±2.9 min after $\tau_{area}$, $n$=9; Fig. S9A) reduced at similar times, indicating that the strong reduction in E-Cad levels during apoptosis is insensitive to the expression level of E-Cad.

The other major components of AJs, α- and β-catenin, behaved similarly to E-cad (Fig. S9B,C). Flies expressing a β-cat homolog fusion construct, Armadillo::YFP, or a *D*α-catenin::RFP fusion marker both showed a reduction of these components (Fig. S9B,C; Movies 7, 8) at the same time that the level of E-cad decreased

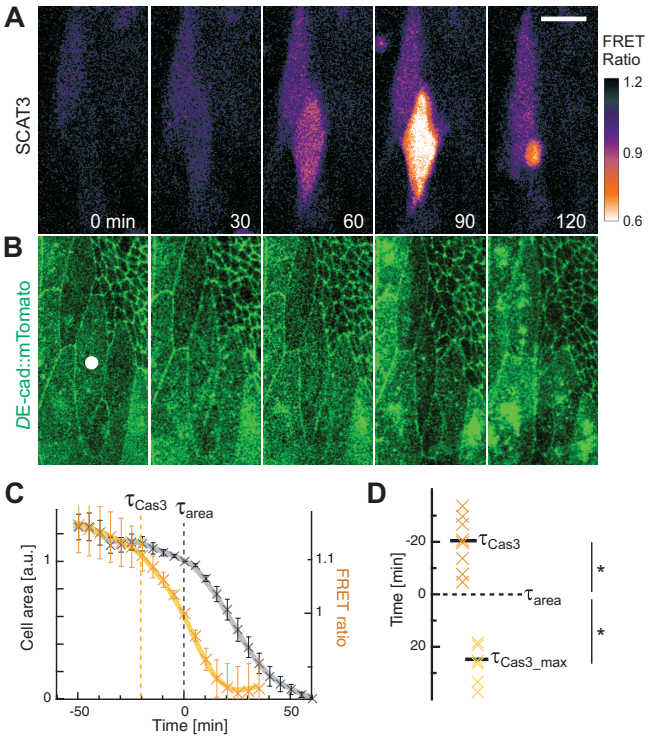


**Fig. 2. Caspase activation precedes apical constriction in apoptotic LECs.** (A,B) Confocal images of wild-type pupa expressing the FRET-based caspase-3 sensor SCAT3 and *D*E-cad::mTomato (Movie 5). Imaging started at 0 min. (A) Stills from a time-lapse movie showing caspase activity in LECs. The pseudocolor represents the fluorescence intensity ratio (Venus/ECFP). (B) Stills from a time-lapse movie of E-cad. An apoptotic LEC is highlighted with a filled circle. (C) Graphs plotting the normalized cell apical area (gray) and caspase-3 activity (orange) of the apoptotic cell over time ($n$=8). Black and orange dashed lines represent $\tau_{area}$ and the time when the cell started to show a higher FRET ratio, $\tau_{Cas3}$, respectively. Error bars indicate s.e.m. (D) Time delays between $\tau_{area}$ and either $\tau_{Cas3}$ or the time caspase reaches its maximum value ($\tau_{Cas3\_max}$) ($n$=8, *$P$<0.05). Average values are shown as thick horizontal lines. Scale bar: 20 µm.

(Fig. S9A; $\tau_{β\text{-}cat\_red}$ and $\tau_{α\text{-}cat\_red}$). To test the possibility that the reduction in the levels of E-cad from AJs is associated with cleavage of β-cat at AJs by caspase-3 (Kessler and Muller, 2009), we used a fly line that replaced endogenous *D*E-cad with a GFP-tagged E-cad-α-cat fusion protein (*D*E-cad-α-cat::GFP) (Morais-de-Sá and Sunkel, 2013). Similar to E-cad, the level of this fusion protein was reduced during extrusion (Fig. S9A,D). This suggests that it is the cleavage of β-cat from a cytoplasmic pool of the protein, rather than the β-cat linking E-cad with α-cat in AJs, that plays a role in the reduction of E-cad. Moreover, we cannot rule out the possibility that the reduction in the levels of E-cad is due to the cleavage of the cytoplasmic region of E-cad by caspase-3 (Bannerman et al., 1998).

The observation that two myosin cables form when E-cad is reduced, suggests a loosening of E-cad-dependent cell-cell adhesion. To follow the kinematics of cell-cell contacts during apoptotic cell extrusion, we visualized the overall plasma membrane using the PH domain of PLCγ (Phosphoinositide phospholipase C, γ form) fused to GFP (PH::GFP) together with MyoII::mCherry. The plasma membranes of apoptotic and neighboring cells sometimes, but not always, detached at the apical section of the cell once the separation of the two myosin cables became apparent (Fig. 3G; Fig. S10). In this case, the myosin cables of each cell were approximately at the edge of plasma membranes (Fig. 3G′). By contrast, the two plasma membranes of apoptotic and neighboring cells could maintain their

Development (2017) 144, 95-105 doi:10.1242/dev.139865

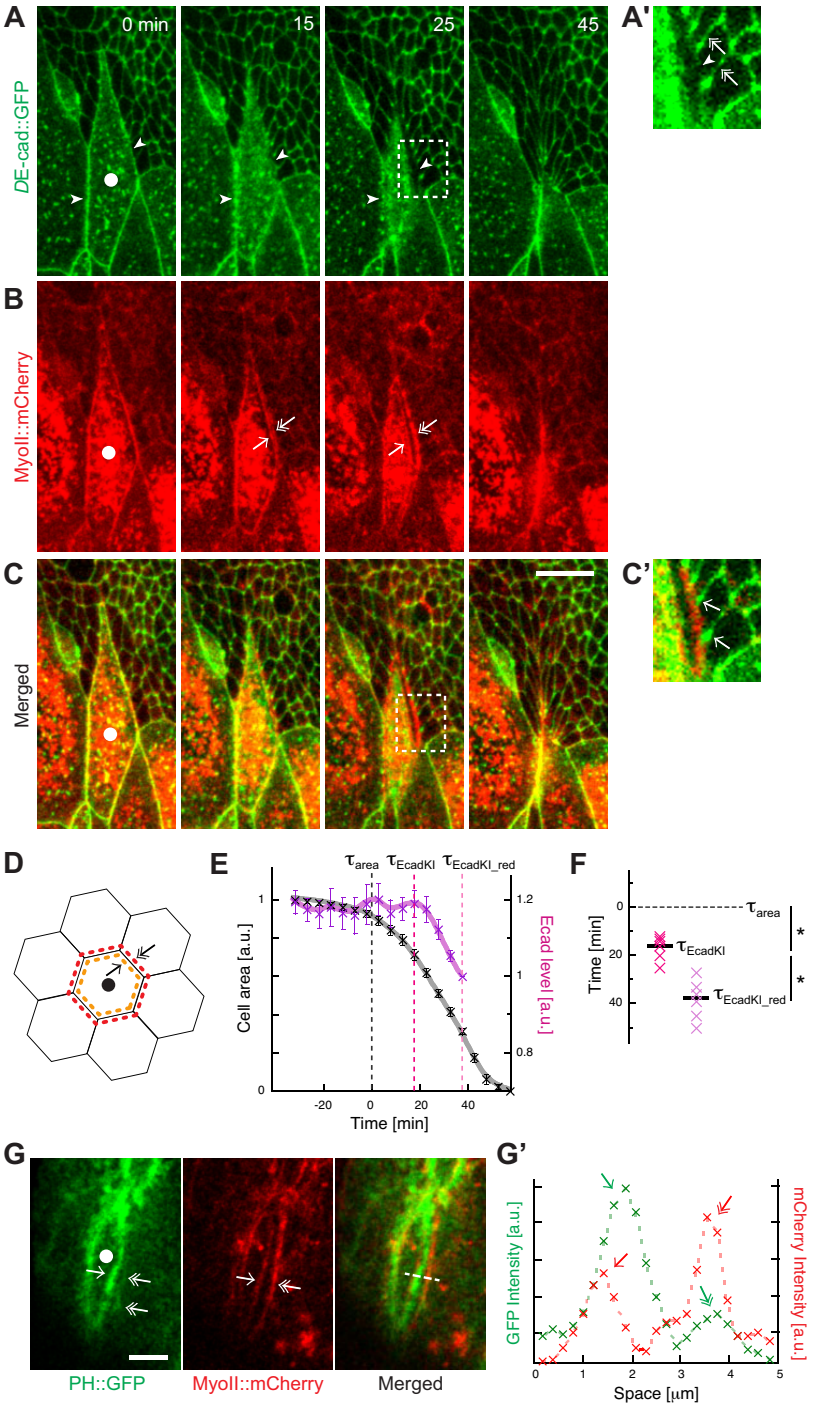


**Fig. 3. Reduction of E-cad levels and AJ remodeling during apical constriction of apoptotic LECs.** (A-C) Confocal images of a wild-type pupa expressing *D*E-cad::GFP and MyoII::mCherry (Movie 6). (A) The progression of E-cad reduction at the interface between the apoptotic LEC and neighboring cells (arrowheads). (A′) High magnification of the boxed region in A. E-cad at cell junctions away from the interface (double arrows) was not reduced. (B) MyoII distribution around the periphery of the apoptotic LEC shows two myosin cable-like structures (arrows and double arrows). (C) Merged images of A and B. (C′) High magnification of the boxed region in C. Arrows show the high accumulation of E-cad at the boundaries between neighboring cells. (D) Schematic (not to scale) showing the actomyosin cable in an apoptotic cell (inner cable; orange dashed line, arrow) and the supra-cellular actomyosin cable in neighboring cells (outer cable; red dashed line, double arrow). (E) Graphs plotting the normalized apical area (gray) and E-cad level (purple) of apoptotic cells of a wild-type pupa expressing *D*E-cad::GFP$^{KI}$, over time ($n$=6). Error bars indicate s.e.m. Black, purple and pink dashed lines denote $\tau_{area}$, the time E-cad starts to decrease ($\tau_{EcadKI}$) and the timing of the strong reduction of E-cad levels ($\tau_{EcadKI\_red}$), respectively. (F) Time delays between $\tau_{area}$ and either $\tau_{EcadKI}$ or $\tau_{EcadKI\_red}$ ($n$=6, *$P$<0.05). Average values are shown as thick horizontal lines. (G) Confocal images of a wild-type pupa expressing the plasma membrane markers PH::GFP and MyoII::mCherry, highlighting the locations of the plasma membrane and myosin cable of the apoptotic cell (arrow) and of the neighboring cells (double arrows). (G′) Line profile of the fluorescence intensity of PH::GFP (green) and MyoII::mCherry (red). The two peaks represent the fluorescence in the apoptotic cell (arrows) and neighboring cell (double arrows). Apoptotic LECs are highlighted with filled circles. Scale bars: 20 µm.

contacts even when the two myosin cables became apparent (Fig. S11).

To gain insight into the dynamics of cell-cell contacts at the basolateral section of the cell, we analyzed the behavior of septate junctions (SJs). These are positioned basal to AJs in *Drosophila* in an opposite orientation relative to that of tight junctions, the functional equivalent of SJs in vertebrates (Oda and Takeichi, 2011). We imaged pupae expressing GFP-tagged Neuroglian, a cell surface trans-membrane protein essential for SJ function (Nrg::GFP). In contrast to AJs, SJs were stable throughout the apical constriction (Fig. S12; Movie 9). This suggests that the permeability barrier function is preserved at SJs even when AJs are disengaged during apoptosis of LECs.

Together, our results show that the AJs between dying cells and their neighbors rearranged during apoptosis, and that this is associated with a reduction in the levels of AJ components.

### MyoII accumulates in apoptotic and neighboring cells at different times during apoptosis

To characterize further the formation of actomyosin cables in apoptotic LECs (inner cable), or in neighboring cells (outer cable), we quantified the temporal progression of MyoII accumulation in pupae expressing GFP-tagged MyoII (MyoII::GFP), in either histoblasts by *esg*-GAL4, or LECs by *Eip71CD*-GAL4 (Fig. 4). These flies also ubiquitously expressed MyoII::mCherry. In GFP-positive histoblasts, which were considered non-dying neighboring

Development (2017) 144, 95-105 doi:10.1242/dev.139865

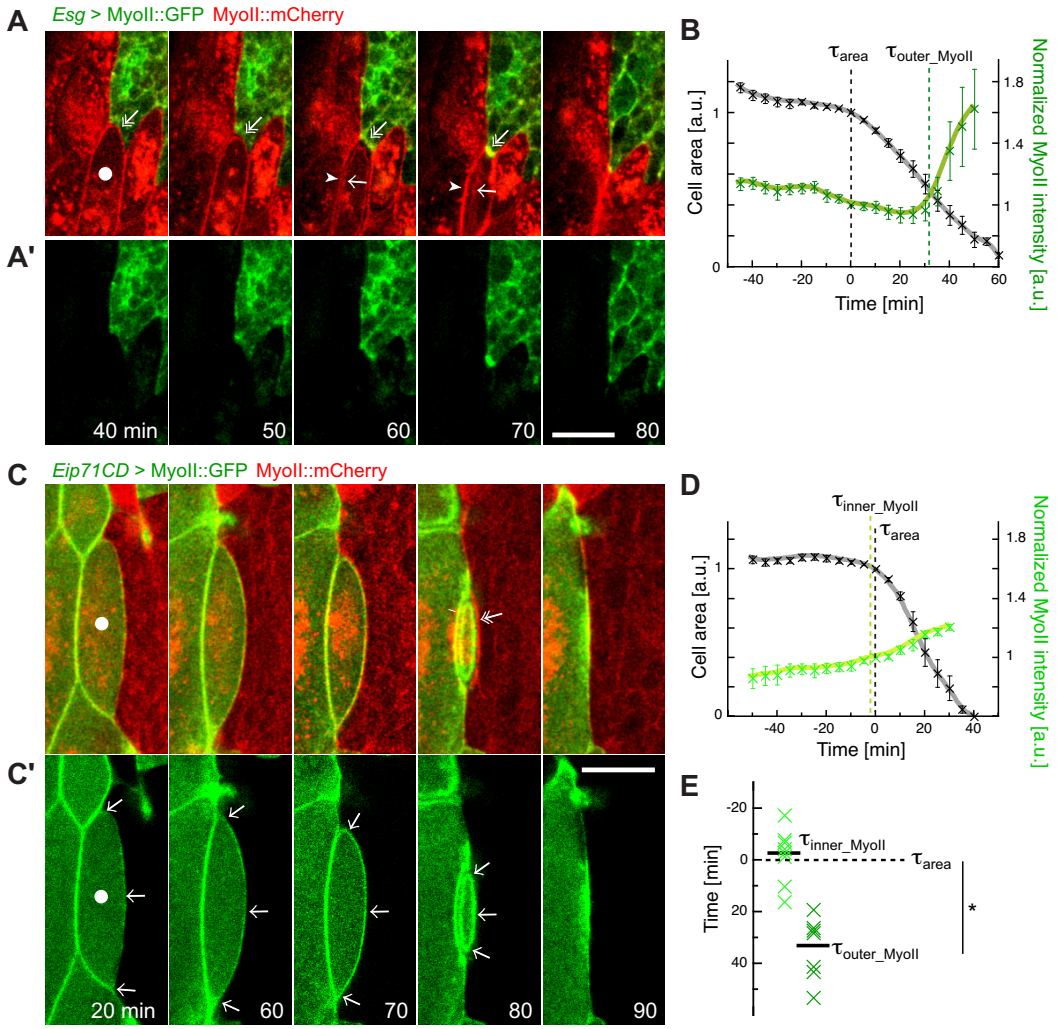


**Fig. 4. MyoII accumulates at different times in apoptotic and neighboring cells.** (A,A′) Confocal images of a wild-type pupa expressing MyoII::GFP only in histoblasts and MyoII::mCherry ubiquitously (Movie 10). (A) Arrows and arrowheads show MyoII accumulation in the apoptotic LEC and in the neighboring LECs, respectively. (A′) MyoII::GFP images. (B) Graph showing the normalized cell area of dying LECs (gray) and MyoII intensity of neighboring histoblast cells (green) over time ($n$=9). Black and green dashed lines denote $\tau_{area}$ and $\tau_{outer\_MyoII}$ (the time when the cell started to accumulate MyoII at a higher rate), respectively. (C,C′) Confocal images of a wild-type pupa expressing MyoII::GFP only in LECs and MyoII::mCherry ubiquitously (Movie 11). (C) The double arrow indicates MyoII accumulation in histoblasts attached to the apoptotic LEC. (C′) MyoII::GFP images. Arrows indicate the region where MyoII intensity in the apoptotic cell was analyzed. (D) Graphs plotting the normalized apical area (gray) and MyoII intensity (green) of an apoptotic cell ($n$=8). Black and green dashed lines denote $\tau_{area}$ and $\tau_{inner\_MyoII}$ (the time when the cell started to accumulate MyoII at a higher rate), respectively. (E) Time delays between $\tau_{area}$ and either $\tau_{Inner\_MyoII}$ ($n$=8) or $\tau_{Outer\_MyoII}$ ($n$=9). *$P$<0.05. Average values of data are shown as thick horizontal lines. Apoptotic LECs are highlighted by filled circles. Error bars indicate s.e.m. Scale bars: 20 µm.

cells, MyoII::GFP was found to accumulate within the vicinity of the apoptotic boundary LECs (Fig. 4A, double arrows; Movie 10). This accumulation commenced when the space between the two MyoII cables became apparent (t=60; Fig. 4A, arrowhead and arrow) and increased with time (Fig. 4B). The time when MyoII started to accumulate, $\tau_{outer\_MyoII}$, was 35.7±3.8 min after $\tau_{area}$ ($n$=9; Fig. 4E; Materials and Methods), which was not significantly different from the timing of E-cad reduction. This indicated that the initiation of MyoII accumulation in neighboring cells coincided with remodeling of AJs. Moreover, the intensity of MyoII in neighboring LECs increased concurrently with MyoII in histoblasts (t=60 and 70; Fig. 4A, arrowheads), suggesting that the formation of actomyosin cables in the two different cell types (i.e. non-dying histoblasts and LECs) was coordinated. To facilitate the analysis of MyoII accumulation in apoptotic LECs, we quantified the intensity of the MyoII::GFP signal (Fig. 4C; Movie 11) that originated solely from the cell periphery of apoptotic LECs facing histoblasts (Fig. 4C′, arrows). In dying cells, MyoII started increasing as apical constriction commenced ($\tau_{inner\_MyoII}$; Fig. 4D,E). This observation implied that the actomyosin cable in the apoptotic cell is present before the reduction of E-cad levels.

Altogether, the analyses of MyoII distribution showed that the formation of actomyosin cables in apoptotic and neighboring cells occur at different times, implying that the two cables are involved in different stages of apoptotic cell extrusion.

### Actomyosin cable formation, apical constriction, and a reduction in E-cad levels upon apoptosis are caspase-3 dependent

In apoptotic LECs, caspase-3 is activated prior to the initiation of apical constriction (Fig. 2), the reduction in E-cad levels (Fig. 3) and the accumulation of MyoII in dying and neighboring cells (Fig. 4).

Development (2017) 144, 95-105 doi:10.1242/dev.139865

To investigate the role of caspase-3 in apoptotic cell extrusion, we ectopically expressed a baculovirus caspase inhibitor, p35, in the majority of LECs by *Eip71CD*-GAL4. This fly also ubiquitously expressed *D*E-cad::GFP$^{KI}$ or MyoII::GFP. As previously reported (Ninov et al., 2007), tissue expansion (Fig. S13A) and the extrusion of LECs are delayed when p35 is expressed, with cells requiring more time to leave the tissue (Fig. 5A; Movie 12; Fig. 5B, pink line). The number of LECs undergoing extrusion was reduced by more than 90%; however, extrusion did not cease completely (38.7±3.3 and 3.0±1.0 cells within 5 h in wild-type and p35 pupae, respectively). During extrusion of p35-positive LECs, no significant reduction in E-cad levels (Fig. 5A; Fig. 5B, blue line) was observed. Similarly, MyoII did not further accumulate in either the extruding or neighboring cells (Fig. 5C-D; Fig. S13B; Movie 13), and the space between MyoII cables (Fig. 5C) was not observed. These results indicated that the extrusion of p35-expressing LECs is different in nature to that of caspase-positive wild-type LECs. Indeed, Ninov et al. reported that extruded p35-positive cells were viable under the epithelium, and were not engulfed by hemocytes (Ninov et al., 2007). We speculate that the extrusion of p35-positive LECs occurs when they are pushed out by expanding histoblasts (Fig. 1E). Together, our data showed that the formation of actomyosin cables, the apical constriction, and the reduction in E-cad levels observed during wild-type LEC apoptosis are caspase dependent.

### Disruption of MyoII compromises apoptotic cell extrusion, without preventing reduction of E-cad levels

To investigate further the mechanism behind the strong reduction in E-cad levels and to define the contribution of actomyosin contractility in this mechanism, we ectopically expressed *sqh*-RNAi (MyoII regulatory light chain RNAi) in the majority of LECs by *Eip71CD*-GAL4. This fly also ubiquitously expressed either *D*E-cad::GFP$^{KI}$ or MyoII::GFP (Fig. 6). The level of MyoII::GFP (Fig. 6A,B) and

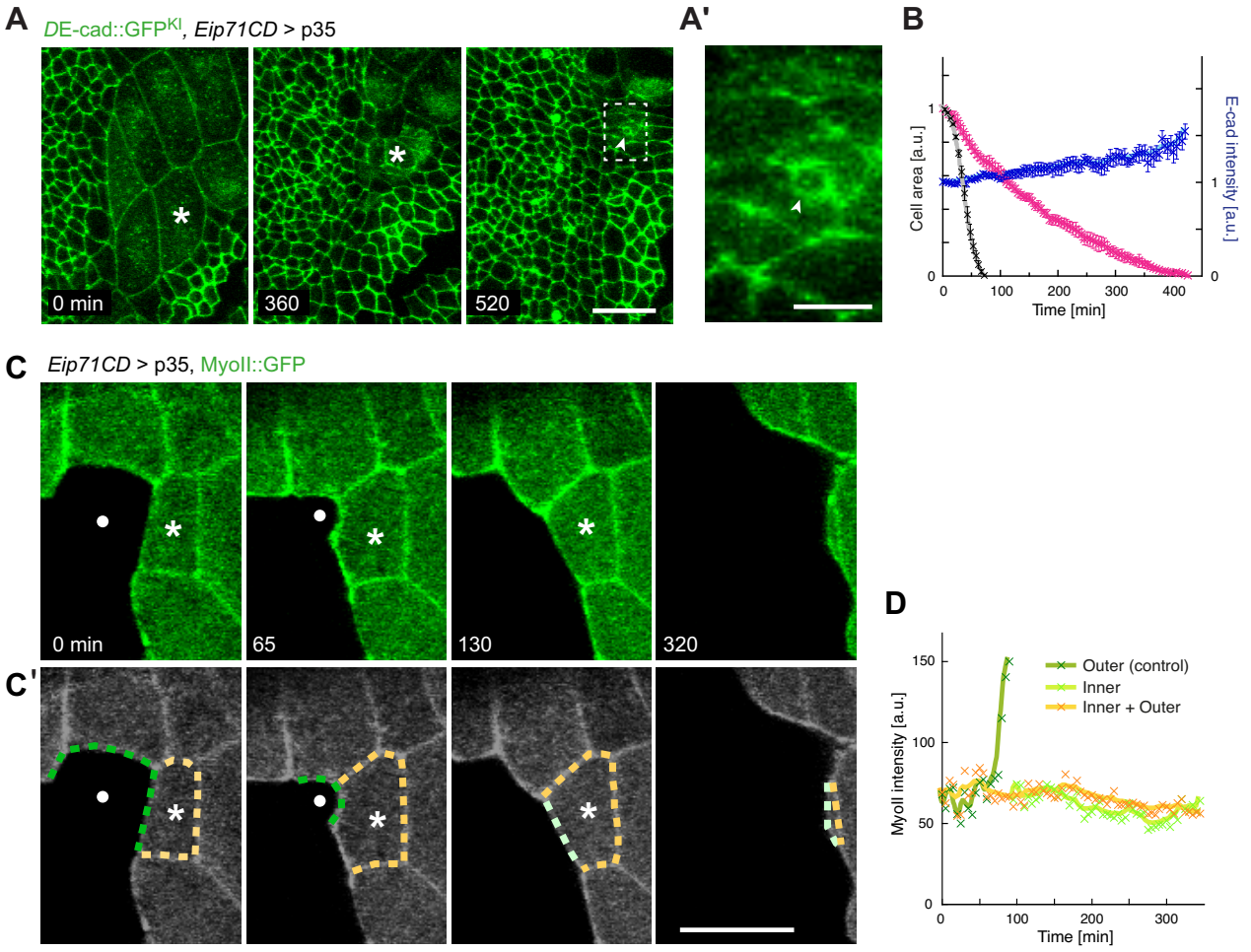


**Fig. 5. Extrusion of LECs expressing the caspase inhibitor p35 is distinct from that of wild-type LECs.** (A) Confocal images of a pupa expressing the caspase inhibitor p35 only in LECs and *D*E-cad::GFP$^{KI}$ ubiquitously (Movie 12). (A′) High magnification of the boxed region in A. Asterisks denote p35-positive delaminating LECs. E-Cad around a delaminating LEC was not reduced throughout apoptosis (arrowhead). (B) Graph plotting normalized cell apical area (pink) and E-cad level (blue) of extruding p35-expressing LECs over time ($n$=7). Error bars indicate s.e.m. Normalized apical cell area of wild-type apoptotic cells (gray, $n$=20) is shown for comparison. (C) Confocal images of a pupa expressing the caspase inhibitor p35 and MyoII::GFP only in LECs. An extruding p35-positive LEC is highlighted with asterisks, and a wild-type apoptotic cell not expressing p35 and MyoII::GFP is highlighted by a filled circle. (C′) Dashed lines denote where MyoII intensity was analyzed for the images in C. Dark green lines highlight the cell boundaries of LECs next to the wild-type apoptotic LEC (indicated by a filled circle), which represent the outer ring. Orange lines highlight the cell boundaries shared by both p35-positive delaminating LECs (asterisk) and non-delaminating LECs (inner+outer ring). Light green lines highlight the cell boundaries of p35-positive delaminating LECs (asterisk; inner ring). Imaging started at 0 min. (D) Graphs plotting MyoII intensities along three different lines shown in C′ over time. Scale bars: 20 µm (A,C′); 10 µm (A′).

Development (2017) 144, 95-105 doi:10.1242/dev.139865

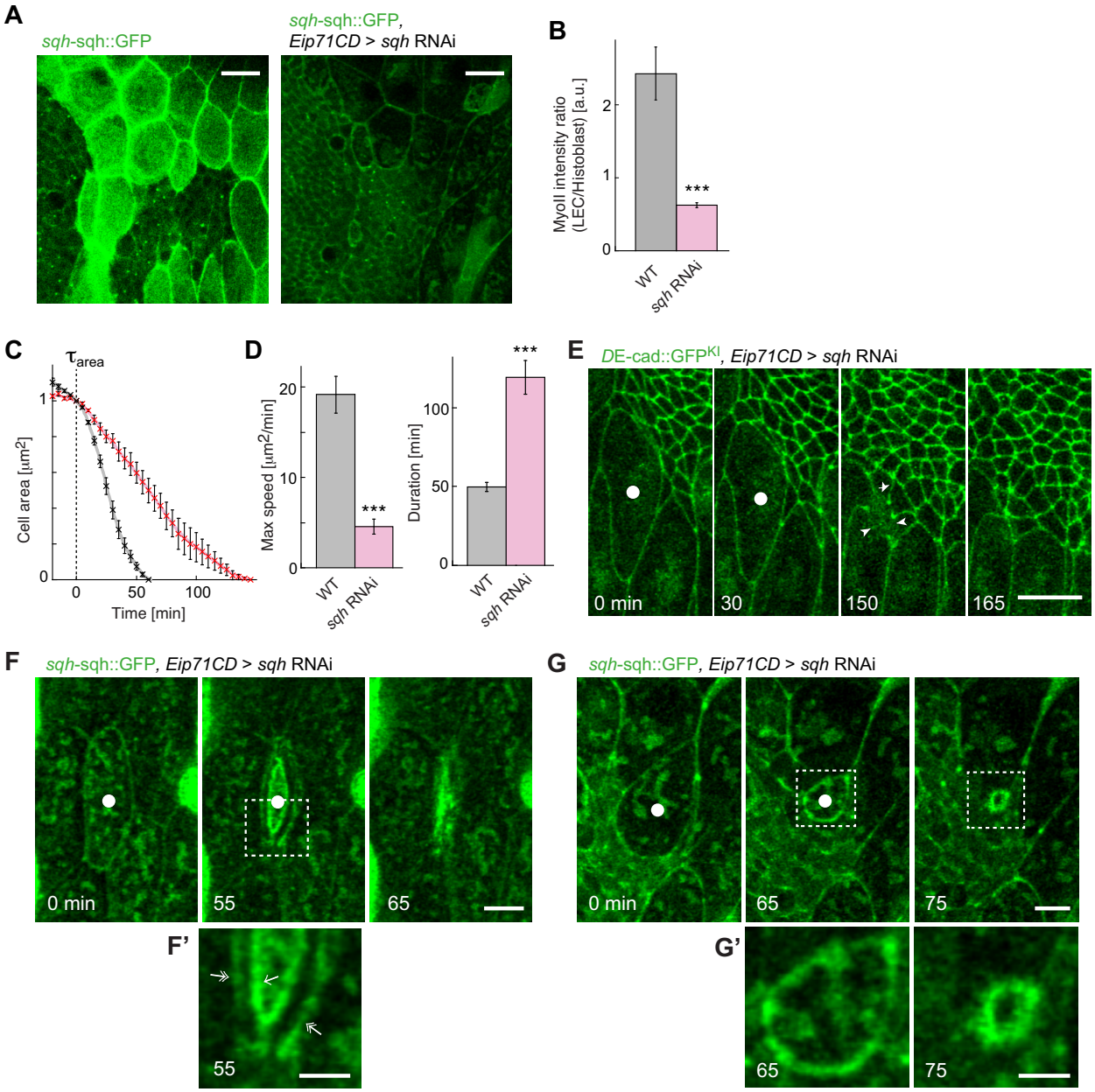


**Fig. 6. Apoptotic cell extrusion in *sqh*-RNAi-expressing LECs.** (A) Confocal images of a wild-type pupa expressing MyoII::GFP ubiquitously (left) and a pupa expressing *sqh*-RNAi only in LECs and MyoII::GFP ubiquitously (right). The contrast of the images was adjusted so that the fluorescence intensity of histoblasts became equivalent. (B) Statistical comparison of the ratio of MyoII intensity between LECs and histoblasts. Gray and pink bars denote the mean values from wild-type (WT) and *sqh*-RNAi-expressing LECs, respectively ($n$=6 and 7 pupae). Each ratio was calculated based on the average of 20 cell boundaries of LECs and histoblasts from an image. (C) Graph plotting the normalized apical cell area of wild-type (gray, $n$=20) and *sqh*-RNAi-positive (pink, $n$=5) apoptotic cells over time. $\tau_{area}$ denotes the time when the cell started to constrict at a higher speed. (D) Statistical comparison of the maximum speed of apical constriction (left) and the duration from $\tau_{area}$ to the completion of apical constriction (right). Gray and pink bars denote the mean values from WT and *sqh*-RNAi-positive LECs, respectively ($n$=20 and 5). (E-G) Confocal images of a pupa expressing *sqh*-RNAi only in LECs, and *D*E-cad::GFP$^{KI}$ (E) or MyoII::GFP (F,G) ubiquitously. (E) A cell undergoes apoptosis and shows a reduction of E-cad levels (arrowheads) (Movie 14). (F,G) Confocal images of apoptotic cells with the space between MyoII cables (F) and without the space (G). (F′,G′) High magnification of the boxed regions in F and G. Arrow and double arrows in F′ show the myosin in an apoptotic cell and in neighboring cells, respectively. Imaging started at 0 min. Extruding *sqh*-RNAi-positive LECs are highlighted by filled circles. ***$P$<0.001. Error bars indicate s.e.m. Scale bars: 20 μm (A); 10 μm (E-G); 5 μm (F′,G′).

phosphorylated myosin regulatory light chain (Fig. S14) in LECs was reduced in *sqh*-RNAi-expressing pupae compared with wild-type pupae. This was accompanied by a strongly delayed apical constriction (Fig. 6C,D), a low level of E-cad in the LECs (Fig. S15), and less, or absence of, mechanical impact on the surrounding histoblasts (Fig. S1B), compared with wild-type pupae. We observed a strong reduction of E-cad in all *sqh*-RNAi-positive apoptotic cells ($n$=9; Fig. 6E, arrowheads; Movie 14). Furthermore, we noticed a space existed between MyoII cables (Fig. 6F; $n$=10 out of 19 cells) in around half of the apoptotic cells whereas in the other apoptotic cells this space was not observed (Fig. 6G; $n$=9 out of 19 cells). Together, these results suggest that the strong reduction of E-cad in apoptotic LECs could be independent of actomyosin cable contraction, whereas the formation of the space between actomyosin

Development (2017) 144, 95-105 doi:10.1242/dev.139865

cables, which was normally observed during wild-type LEC apoptosis, required actomyosin contractility.

### Disruption of MyoII in neighboring cells strongly delays apoptotic cell extrusion

To understand the role of the supra-cellular actomyosin cable in apoptotic cell extrusion, we sought to impair actomyosin contractility only in neighboring non-dying cells. To this end, we expressed *sqh*-RNAi in a subset of LECs using the mosaic analysis with a repressible cell marker (MARCM) system (Lee and Luo, 1999) (Fig. 7A-B′; Movie 15). We then examined apoptosis of wild-type LECs, which were positioned next to RNAi-positive LECs (Fig. 7B, blue dotted outlines). In this case, all but one of the neighboring cells were wild type, and the contractility of the supra-cellular actomyosin cable was therefore only partially affected. First, we qualitatively compared the apical constriction of apoptotic wild-type LECs that were next to RNAi-positive cells (hereafter referred to as $LEC_{WT/RNAi}$; Fig. 7B, red dotted outlines) with that of wild-type LECs fully surrounded by wild-type cells (hereafter referred to as $LEC_{WT/WT}$; Fig. 7B, white dotted outlines). This comparison was performed on cells in the same pupa. We found that LECs with MyoII-defective neighbors ($LEC_{WT/RNAi}$) exhibited a slower apical constriction, which, compared with controls, also required a longer time to complete (Fig. 7C). Quantitative analyses further supported these observations (Fig. 7D) and we reasoned that this delay was the result of the partially compromised supra-cellular actomyosin cable in neighboring cells. The contour plot of the apoptotic $LEC_{WT/RNAi}$ shown in Fig. 7B shows that the apical constriction appears to be biased toward the RNAi-positive cell (Fig. 7E, arrow). This observation was further supported by tracking the trajectory of the centroid of the apoptotic cell shape (Fig. 7F,F′). These observations suggested that supra-cellular actomyosin cables with partially defective myosin contraction lead to eccentric deformation of apoptotic cells. Together, our data showed that the actomyosin cable that formed in neighboring cells upon apoptosis plays an important role in the extrusion process.

### Tissue tension is transiently released upon E-cad reduction and rebuilt afterwards

The appearance of two actomyosin cables associated with a reduction in E-cad level implied that tissue tension is altered during the apoptotic cell extrusion. Indeed, we found that a subset of neighboring histoblast cell boundaries, which are orthogonal to the interface between apoptotic and neighboring cells, lose their

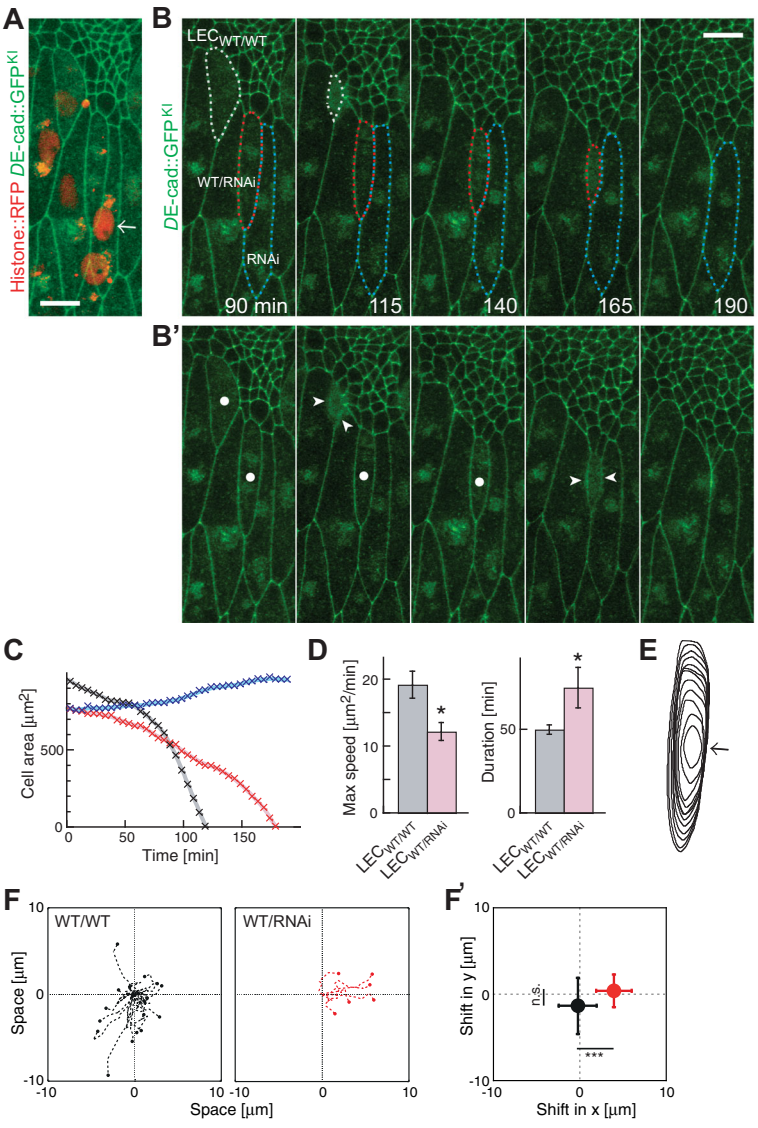


**Fig. 7. Clonal disruption of MyoII in neighboring cells compromises apoptotic cell extrusion.** (A) Confocal image of a pupa expressing *sqh*-RNAi in a subset of LECs. LECs with bright (two copies of) Histone::RFP represent LECs expressing *sqh*-RNAi (white arrow); this is distinct from the control cells, which either lacked Histone-RFP, or expressed only a single copy. The pupa also expresses *D*E-cad::GFP$^{KI}$. (B,B′) Stills from a time-lapse movie of the pupa shown in A (Movie 15). (B) The cell highlighted with a blue dotted line is an LEC expressing *sqh*-RNAi ($LEC_{RNAi}$). The cell highlighted with a red dotted line is a wild-type LEC next to an RNAi-positive LEC ($LEC_{WT/RNAi}$). The cell highlighted with a white dotted line is a wild-type LEC surrounded by wild-type histoblasts and LECs ($LEC_{WT/WT}$). The genotype of the three different cells can be found in Materials and Methods. (B′) Both $LEC_{WT/RNAi}$ and $LEC_{WT/WT}$ undergo apoptosis and show a reduction of E-cad levels (arrowheads). (C) Graph showing the apical cell area of the apoptotic $LEC_{WT/WT}$ (black), apoptotic $LEC_{WT/RNAi}$ (red) and neighboring $LEC_{RNAi}$ (blue). (D) Statistical comparison of the maximum speed of apical constriction and the duration from $\tau_{area}$ to the completion of apical constriction. Gray and pink bars denote the mean values from $LEC_{WT/WT}$ and $LEC_{WT/RNAi}$, respectively ($n$=58 and 6). (E) Contour plots showing the apical cell shape change of the apoptotic $LEC_{WT/RNAi}$ highlighted in B over time. The constriction appears to be biased toward the RNAi-positive cell (arrow). (F) Trajectory of the centroid of apoptotic cell shape after $\tau_{area}$. Trajectories of $LEC_{WT/WT}$ cells ($n$=20) and $LEC_{WT/RNAi}$ cells ($n$=6) are shown in black and red, respectively. For the analysis of $LEC_{WT/RNAi}$ cells, the images were rotated so that the RNAi-positive cell was placed to the right of the apoptotic cell. (F′) Statistical comparison of the end point of the trajectory shown in F. Error bars indicate s.e.m. *$P$<0.05; ***$P$<0.001; n.s., not significant. Scale bars: 20 µm.

Development (2017) 144, 95-105 doi:10.1242/dev.139865

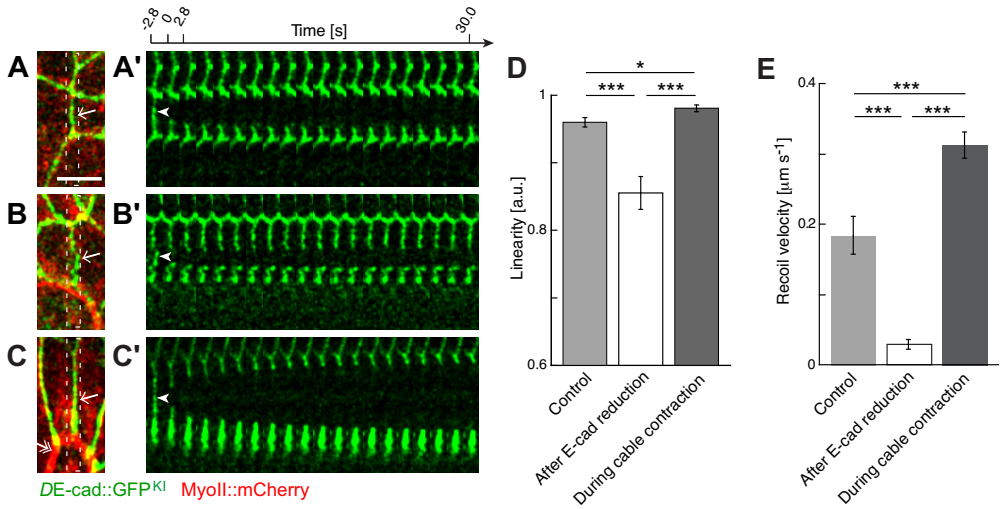


**Fig. 8. Tissue tension release and re-shape after reduction of E-cad levels.** (A-C) Confocal images of wild-type pupae expressing *D*E-cad::GFP$^{KI}$ and MyoII::mCherry ubiquitously highlighting the histoblast cell boundaries connected to the apoptotic LEC (arrows) before laser ablation. (A′-C′) Kymographs generated from the regions within the dashed lines in A-C, showing the dynamics of the cell boundaries after ablation (Movie 16). The laser ablations (arrowheads) were performed at three different stages of apoptotic cell extrusion: before reduction of E-cad levels (A,A′); right after reduction (B,B′); and during neighboring actomyosin cable (double arrow in C) contraction (C,C′). Scale bar: 5 µm. (D,E) Statistical comparison of the cell boundary linearities (D) and the recoil velocities (E) at each stage of cell extrusion shown in A-C. *n*=17, 12 and 27 for control, after reduction, and, during cable contraction, respectively. Error bars indicate s.e.m. **P*<0.05; ****P*<0.001.

straightness (Fig. 8A,B, arrows), suggesting a release of junctional tension. We also noticed that the cell boundary became straight again (Fig. 8C, arrow) when the outer cable contracted (Fig. 8C, double arrow). Quantification of the linearity of the cell boundaries (Materials and Methods) further supported these observations (Fig. 8D). To characterize the change in tension of neighboring cells during apoptosis, we probed the junctional tension at different stages of apoptosis by laser nano-ablation (Hara et al., 2016) (Fig. 8A′-C′; Movie 16). Compared with the control boundaries, the initial recoil velocity after ablation (Materials and Methods), which is the first good approximation of the junctional tension right before ablation, decreased immediately after E-cad levels decreased (Fig. 8E). Moreover, the initial recoil velocity of the junction vertices increased to an even higher level at the later stages of apoptosis, compared with that of the control boundaries (Fig. 8E). The cell boundaries of neighboring LECs showed the same trend (Fig. S16). Altogether, our results show that tissue tension is transiently released upon reduction of E-Cad and is rebuilt during the late stages of cell extrusion.

## DISCUSSION

### Progressive remodeling of AJs and redistribution of tensile force upon apoptosis

We report here the temporal sequence of events during apoptotic cell extrusion, with a focus on the remodeling of AJs, the cytoskeleton, and mechanical tension. After caspase-3 starts to be activated in LECs, those undergoing apoptosis initiate apical constriction (Fig. 2). We reasoned that the initiation of this constriction could be due to a combination of actomyosin cable formation in the dying cell (Fig. 4) and the activity of caspase-3, which assists in the upregulation of actomyosin contractility. Indeed, it has been shown in tissue culture that cleavage of Rho associated kinase by caspase-3 is involved in phosphorylation and activation of myosin light chain, which regulates actomyosin contractility (Leung et al., 1996). We propose that the actomyosin cable that forms in apoptotic LECs is responsible for the early stages of apoptotic cell extrusion. During apical constriction, the level of AJ components, including E-cad, strongly reduced in a caspase-3-dependent manner (Fig. 5). In the neighboring non-dying cells, this reduction is found only at the interface between the apoptotic cell and its neighbors (Fig. 3A′). As caspase-3 is not activated in the neighboring cells, we speculate that the reduction of E-cad is a consequence of a loss of trans-interactions between E-cad in the neighboring cell and E-cad in the apoptotic cell, which undergoes caspase-3-dependent cleavage. This often, but not always, leads to plasma membrane separation (Fig. 3G), which is suggestive of a loosening of AJ-dependent adhesion. Reyes et al. reported that anillin organizes and stabilizes actomyosin contractile rings at AJs and its knockdown is associated with a reduction of E-cad and β-cat levels at AJs, leading to AJ disengagement (Reyes et al., 2014). A gradual decrease in the level of E-cad (Fig. 3E) and a gradual increase in MyoII accumulation in apoptotic cells (Fig. 5D) was observed prior to the strong reduction of E-cad levels. This leads us to hypothesize that mechanical tension exerted on the cell interface between apoptotic LECs and neighboring cells by the contraction of the actomyosin cable, which forms in the apoptotic cell, is large enough to rupture the weakened contacts between plasma membranes at AJs upon the strong reduction of E-cad levels. Interestingly, and by contrast, there are cases when AJs are not disengaged even after the level of E-cad is reduced. In these cases, the cells exhibit a separation of actomyosin cables from the membrane (Fig. S11). We speculate that the state of cell-cell contacts at AJs, i.e. whether they will disengage or remain engaged during apoptosis, is dependent on which of the following links is weaker: the link between two plasma membranes, or the link between the plasma membrane and the actomyosin cable. Both of these links would be weakened by a strong, albeit incomplete, reduction of E-cad levels. When the former is weaker than the latter, the two plasma membranes could be detached. When the former is stronger than the latter, the two plasma membranes could remain in contact, and the actomyosin cable could be detached from the plasma membrane.

In parallel with the reduction of E-cad levels and the associated release of tension (Fig. 8), a supra-cellular actomyosin cable begins

Development (2017) 144, 95-105 doi:10.1242/dev.139865

to form in neighboring cells (Fig. 4). These observations prompt us to speculate that the release of tissue tension triggers MyoII accumulation in neighboring cells. Subsequent contraction of this outer ring helps to re-shape tissue tension, which is transiently released when E-cad is reduced. As a consequence, the neighboring cells are stretched (Fig. 1). Upon completion of apical constriction, neighboring non-apoptotic cells form *de novo* AJs (Fig. S8) and the stretched cells undergo cell division and/or cell-cell contact rearrangement (Fig. S2). These processes allow a relaxation of the high tension associated with the stretching of cells (Fig. 7E). Finally, our measurements of caspase-3 activity (Fig. 2), and our observations from caspase inhibition experiments (Fig. 5), help us to conclude that the characteristics associated with apoptotic cell extrusion reported in this study are the consequences of the apoptotic process, rather than the cause.

### Apoptosis mechanically drives tissue expansion

In addition to the progressive remodeling of AJs and modulation of tissue tension during apoptosis, we examined the mechanical role of apoptosis 'apoptotic force' in tissue morphogenesis, which has been proposed, demonstrated and discussed previously (Stenn et al., 1998; Toyama et al., 2008; Suzanne et al., 2010; Teng and Toyama, 2011; Miura, 2012; Kuranaga, 2012; Monier et al., 2015; Okuda et al., 2016; Pérez-Garijo and Steller, 2015; Monier and Suzanne, 2015; Ambrosini et al., 2016). We show that the mechanical force generated by the contraction of actomyosin cables formed when LECs undergo apoptosis, especially boundary LECs, promotes tissue expansion (Fig. 1; Fig. S1), along with histoblast proliferation and migration (Ninov et al., 2007, 2010). Nonetheless, we cannot rule out the possibility that this apical contraction is in part driven by a decrease in cell volume, which can be triggered by caspase activation (Saias et al., 2015). Intriguingly, we found that apoptosis of non-boundary LECs did not affect tissue expansion (Figs S5, S6). This raised the possibility that the mechanical influence of apoptosis in neighboring tissues is dependent not only on the physical connections between cells but also on the mechanical properties of cells, including cell compliance. If a tissue is soft, for instance, the tensile forces generated by the apoptotic process could be absorbed by nearest-neighbor cells and would not propagate to cells further than a single cell away. We speculate that the apoptotic process could mechanically contribute to cell death-related morphogenesis, but only when apoptosis takes place among a tissue with optimal mechanical properties.

Here, we present a framework for understanding how cell adhesions and tissue tension are progressively modulated during apoptosis in a developing epithelium (Fig. S17). We conclude that tissue tension re-shaping, including the transient release of tension upon a reduction in the levels of AJ components, represents a mechanism of apoptotic cell extrusion. It would be important to explore how this transient modulation in mechanical tension would further influence the biochemical nature of neighboring non-apoptotic cells.

## MATERIALS AND METHODS

### *Drosophila* stains, fly husbandry, sample preparation and live imaging

Fly lines are described in supplementary Materials and Methods. Flies and crosses were raised on standard media at 25°C. Staged pupae were collected, dissected, mounted and imaged as previously described (Ninov and Martín-Blanco, 2007). *z*-stack images were captured every 1.6 µm along the apical-basal axis of the tissue at 5-min intervals (except for Fig. 3D, which was at 2.5-min intervals) using a Nikon A1R MP confocal microscope with an Apo 40× WI λ S DIC N2, N.A 1.25 objective, or a Zeiss LSM 510 Meta inverted confocal microscope with a LD C-Apo 40×, N.A 1.1 objective. All imaging was performed at room temperature.

### Image analyses and quantification

All confocal images shown (except for those in Fig. 8, Fig. S12 and Fig. S16) are maximum projections of ∼3 µm along the apical-basal axis of a cell around AJs. The images shown in Fig. 8, Fig. S12 and Fig. S16 are single confocal sections at AJs. We used ImageJ, Packing Analyzer V2.0 (Aigouy et al., 2010), and/or Matlab software (MathWorks) for image quantification and subsequent analyses. See supplementary Materials and Methods for further details of image quantification and subsequent analyses of cell shape anisotropy, caspase 3 activity, apical constriction timings, MyoII intensity, cell boundary linearity, initial recoil velocity and cell shape deformation.

### Immunohistochemistry

Pupae were staged as described by Ninov and Martin-Blanco (2007), and dissected and fixed following protocols described by Wang and Yoder (2011). DNA was stained with 4′,6-diamidino-2-phenylindole (DAPI). The primary antibody anti-pMLC (Cell Signaling, #3671) was used at 1:50. A secondary antibody was Alexa-546-conjugated donkey anti-rabbit (1:1000, LifeTechnology, A10040).

### Laser ablation

Laser ablation of histoblasts was performed using a Leica TCS SP5 multi-photon confocal microscope with a 63×/1.4-0.6 HCX PL Apo objective. Ablation was carried out at the AJ plane with a multi-photon laser (Mai-Tai HP from Spectra Physics, CA, USA) set to 800 nm, with a laser power of 40% of the 2.8 W maximum output. Further details can be found in Founounou et al. (2013).

Laser ablation of LECs was performed using a femtosecond laser (FP1030 from Fianium, UK) interfaced to a Nikon A1R MP confocal microscope. The laser power was set to 140 mW at the back aperture of the objective. Further details can be found in Hara et al. (2016).

### Statistics

All the *P*-values were calculated using Student's *t*-test with $P<0.05$ considered significantly different.

#### Acknowledgements

We acknowledge the following for the generous gift of flies: M. Affolter, H. Hong, D. P. Kiehart, E. Kuranaga, T. Lecuit, A. C. Martin, M. Miura, K. Sugimura, the Bloomington Stock Center, the Kyoto *Drosophila* Genetic Resource Center and the Vienna *Drosophila* RNAi Center. We thank the Microscopy Core of MBI, the Bioimaging and Biocomputing Facility of TLL and the Microscopy Rennes Imaging Center. We also thank E. Kuranaga, B. Ladoux, E. Martín-Blanco, M. Sheetz, M. Sudol, K. Sugimura and the MBI Science Communication Core (S. Wolf) for helpful discussions and critical reading of the manuscript.

#### Competing interests

The authors declare no competing or financial interests.

#### Author contributions

X.T. and Y.T. designed the research and prepared the manuscript. X.T., R.L.B., and Y.T. edited the manuscript. X.T., R.L.B., and Y.T. performed the experiments and analyses. L.Q. contributed new reagents. Y.T. oversaw the project.

#### Funding

This work was supported by an NUS Research Scholarship from the National University of Singapore (to X.T.); Mechanobiology Institute, Singapore and National University of Singapore Startup Grants (to Y.T.); Temasek Life Sciences Laboratory (Y.T.); and a Ministry of Education - Singapore Tier 2 grant (MOE2015-T2-1-116 to Y.T.). R.L.B. and Y.T. were supported by the PHC Merlion Programme no. 5.14.13 of the Institut Français de Singapour, under administrative supervision of the Ministère des Affaires Étrangères, and the National University of Singapore.

#### Supplementary information

Supplementary information available online at
http://dev.biologists.org/lookup/doi/10.1242/dev.139865.supplemental

Development (2017) 144, 95-105 doi:10.1242/dev.139865

## References


**Aigouy, B., Farhadifar, R., Staple, D. B., Sagner, A., Röper, J.-C., Jülicher, F. and Eaton, S.** (2010). Cell flow reorients the axis of planar polarity in the wing epithelium of Drosophila. *Cell* **142**, 773-786.

**Ambrosini, A., Gracia, M., Proag, A., Rayer, M., Monier, B. and Suzanne, M.** (2016). Apoptotic forces in tissue morphogenesis. *Mech. Dev*. S0925-4773(16) 30050-30058.

**Bannerman, D. D., Sathyamoorthy, M. and Goldblum, S. E.** (1998). Bacterial lipopolysaccharide disrupts endothelial monolayer integrity and survival signaling events through caspase cleavage of adherens junction proteins. *J. Biol. Chem.* **273**, 35371-35380.

**Bischoff, M. and Cseresnyes, Z.** (2009). Cell rearrangements, cell divisions and cell death in a migrating epithelial sheet in the abdomen of Drosophila. *Development* **136**, 2403-2411.

**Brancolini, C., Lazarevic, D., Rodriguez, J. and Schneider, C.** (1997). Dismantling cell–cell contacts during apoptosis is coupled to a caspase-dependent proteolytic cleavage of β-catenin. *J. Cell Biol.* **139**, 759-771.

**Brand, A. H. and Perrimon, N.** (1993). Targeted gene expression as a means of altering cell fates and generating dominant phenotypes. *Development* **118**, 401-415.

**Eisenhoffer, G. T., Loftus, P. D., Yoshigi, M., Otsuna, H., Chien, C.-B., Morcos, P. A. and Rosenblatt, J.** (2012). Crowding induces live cell extrusion to maintain homeostatic cell numbers in epithelia. *Nature* **484**, 546-549.

**Founounou, N., Loyer, N. and Le Borgne, R.** (2013). Septins regulate the contractility of the actomyosin ring to enable adherens junction remodeling during cytokinesis of epithelial cells. *Dev. Cell* **24**, 242-255.

**Hara, Y., Shagirov, M. and Toyama, Y.** (2016). Cell boundary elongation by non-autonomous contractility in cell oscillation. *Curr. Biol.* **26**, 2388-2396.

**Harris, T. J. C. and Tepass, U.** (2010). Adherens junctions: from molecules to morphogenesis. *Nat. Rev. Mol. Cell Biol.* **11**, 502-514.

**Huang, J., Zhou, W., Dong, W., Watson, A. M. and Hong, Y.** (2009). Directed, efficient, and versatile modifications of the Drosophila genome by genomic engineering. *Proc. Natl. Acad. Sci. USA* **106**, 8284-8289.

**Jacobson, M. D., Weil, M. and Raff, M. C.** (1997). Programmed cell death in animal development. *Cell* **88**, 347-354.

**Kessler, T. and Müller, H. A. J.** (2009). Cleavage of Armadillo/beta-catenin by the caspase DrICE in Drosophila apoptotic epithelial cells. *BMC Dev. Biol.* **9**, 15.

**Kiehart, D. P., Galbraith, C. G., Edwards, K. A., Rickoll, W. L. and Montague, R. A.** (2000). Multiple forces contribute to cell sheet morphogenesis for dorsal closure in Drosophila. *J. Cell Biol.* **149**, 471-490.

**Kuipers, D., Mehonic, A., Kajita, M., Peter, L., Fujita, Y., Duke, T., Charras, G. and Gale, J. E.** (2014). Epithelial repair is a two-stage process driven first by dying cells and then by their neighbours. *J. Cell Sci.* **127**, 1229-1241.

**Kuranaga, E.** (2012). Beyond apoptosis: caspase regulatory mechanisms and functions in vivo. *Genes Cells* **17**, 83-97.

**Kuranaga, E., Matsunuma, T., Kanuka, H., Takemoto, K., Koto, A., Kimura, K.-I. and Miura, M.** (2011). Apoptosis controls the speed of looping morphogenesis in Drosophila male terminalia. *Development* **138**, 1493-1499.

**Lecuit, T. and Yap, A. S.** (2015). E-cadherin junctions as active mechanical integrators in tissue dynamics. *Nat. Cell Biol.* **17**, 533-539.

**Lee, T. and Luo, L.** (1999). Mosaic analysis with a repressible cell marker for studies of gene function in neuronal morphogenesis. *Neuron* **22**, 451-461.

**Leung, T., Chen, X. Q., Manser, E. and Lim, L.** (1996). The p160 RhoA-binding kinase ROK alpha is a member of a kinase family and is involved in the reorganization of the cytoskeleton. *Mol. Cell. Biol.* **16**, 5313-5327.

**Levayer, R., Dupont, C. and Moreno, E.** (2016). Tissue crowding induces caspase-dependent competition for space. *Curr. Biol.* **26**, 670-677.

**Lubkov, V. and Bar-Sagi, D.** (2014). E-cadherin-mediated cell coupling is required for apoptotic cell extrusion. *Curr. Biol.* **24**, 868-874.

**Manjón, C., Sánchez-Herrero, E. and Suzanne, M.** (2007). Sharp boundaries of Dpp signalling trigger local cell death required for Drosophila leg morphogenesis. *Nat. Cell Biol.* **9**, 57-63.

**Marinari, E., Mehonic, A., Curran, S., Gale, J., Duke, T. and Baum, B.** (2012). Live-cell delamination counterbalances epithelial growth to limit tissue overcrowding. *Nature* **484**, 542-545.

**Meghana, C., Ramdas, N., Hameed, F. M., Rao, M., Shivashankar, G. V. and Narasimha, M.** (2011). Integrin adhesion drives the emergent polarization of active cytoskeletal stresses to pattern cell delamination. *Proc. Natl. Acad. Sci. USA* **108**, 9107-9112.

**Michael, M., Meiring, J. C. M., Acharya, B. R., Matthews, D. R., Verma, S., Han, S. P., Hill, M. M., Parton, R. G., Gomez, G. A. and Yap, A. S.** (2016). Coronin 1B reorganizes the architecture of F-actin networks for contractility at steady-state and apoptotic adherens junctions. *Dev. Cell* **37**, 58-71.

**Miura, M.** (2012). Apoptotic and nonapoptotic caspase functions in animal development. *Cold Spring Harb. Perspect. Biol.* **4**. a008664.

**Monier, B. and Suzanne, M.** (2015). Chapter twelve-the morphogenetic role of apoptosis. *Curr. Top. Dev. Biol.* **114**, 335-362.

**Monier, B., Gettings, M., Gay, G., Mangeat, T., Schott, S., Guarner, A. and Suzanne, M.** (2015). Apico-basal forces exerted by apoptotic cells drive epithelium folding. *Nature* **518**, 245-248.

**Morais-De-Sá, E. and Sunkel, C.** (2013). Adherens junctions determine the apical position of the midbody during follicular epithelial cell division. *EMBO Rep.* **14**, 696-703.

**Muliyil, S., Krishnakumar, P. and Narasimha, M.** (2011). Spatial, temporal and molecular hierarchies in the link between death, delamination and dorsal closure. *Development* **138**, 3043-3054.

**Nakajima, Y.-I., Kuranaga, E., Sugimura, K., Miyawaki, A. and Miura, M.** (2011). Nonautonomous apoptosis is triggered by local cell cycle progression during epithelial replacement in Drosophila. *Mol. Cell. Biol.* **31**, 2499-2512.

**Ninov, N. and Martín-Blanco, E.** (2007). Live imaging of epidermal morphogenesis during the development of the adult abdominal epidermis of Drosophila. *Nat. Protoc.* **2**, 3074-3080.

**Ninov, N., Chiarelli, D. A. and Martin-Blanco, E.** (2007). Extrinsic and intrinsic mechanisms directing epithelial cell sheet replacement during Drosophila metamorphosis. *Development* **134**, 367-379.

**Ninov, N., Menezes-Cabral, S., Prat-Rojo, C., Manjón, C., Weiss, A., Pyrowolakis, G., Affolter, M. and Martín-Blanco, E.** (2010). Dpp signaling directs cell motility and invasiveness during epithelial morphogenesis. *Curr. Biol.* **20**, 513-520.

**Oda, H. and Takeichi, M.** (2011). Structural and functional diversity of cadherin at the adherens junction. *J. Cell Biol.* **193**, 1137-1146.

**Okuda, S., Inoue, Y., Eiraku, M., Adachi, T. and Sasai, Y.** (2016). Modeling cell apoptosis for simulating three-dimensional multicellular morphogenesis based on a reversible network reconnection framework. *Biomech. Model. Mech*. **15**, 805-816.

**Pérez-Garijo, A. and Steller, H.** (2015). Spreading the word: non-autonomous effects of apoptosis during development, regeneration and disease. *Development* **142**, 3253-3262.

**Reyes, C. C., Jin, M., Breznau, E. B., Espino, R., Delgado-Gonzalo, R., Goryachev, A. B. and Miller, A. L.** (2014). Anillin regulates cell-cell junction integrity by organizing junctional accumulation of Rho-GTP and actomyosin. *Curr. Biol.* **24**, 1263-1270.

**Riedl, S. J. and Shi, Y.** (2004). Molecular mechanisms of caspase regulation during apoptosis. *Nat. Rev. Mol. Cell Biol.* **5**, 897-907.

**Rosenblatt, J., Raff, M. C. and Cramer, L. P.** (2001). An epithelial cell destined for apoptosis signals its neighbors to extrude it by an actin- and myosin-dependent mechanism. *Curr. Biol.* **11**, 1847-1857.

**Saias, L., Swoger, J., D'angelo, A., Hayes, P., Colombelli, J., Sharpe, J., Salbreux, G. and Solon, J.** (2015). Decrease in cell volume generates contractile forces driving dorsal closure. *Dev. Cell* **33**, 611-621.

**Shen, J. and Dahmann, C.** (2005). Extrusion of cells with inappropriate Dpp signaling from Drosophila wing disc epithelia. *Science* **307**, 1789-1790.

**Sokolow, A., Toyama, Y., Kiehart, D. P. and Edwards, G. S.** (2012). Cell ingression and apical shape oscillations during dorsal closure in Drosophila. *Biophys. J.* **102**, 969-979.

**Stenn, K., Parimoo, S. and Prouty, S.** (1998). Growth of the hair follicle: a cycling and regenerating biological system. In *Molecular Basis of Epithelial Appendage Morphogenesis* (ed. C.-M. Chuong), pp. 111-130. Austin, TX: R. G. Landes.

**Suzanne, M., Petzoldt, A. G., Spéder, P., Coutelis, J.-B., Steller, H. and Noselli, S.** (2010). Coupling of apoptosis and L/R patterning controls stepwise organ looping. *Curr. Biol.* **20**, 1773-1778.

**Takeichi, M.** (2014). Dynamic contacts: rearranging adherens junctions to drive epithelial remodelling. *Nat. Rev. Mol. Cell Biol.* **15**, 397-410.

**Takemoto, K., Nagai, T., Miyawaki, A. and Miura, M.** (2003). Spatio-temporal activation of caspase revealed by indicator that is insensitive to environmental effects. *J. Cell Biol.* **160**, 235-243.

**Teng, X. and Toyama, Y.** (2011). Apoptotic force: active mechanical function of cell death during morphogenesis. *Dev. Growth Differ.* **53**, 269-276.

**Toyama, Y., Peralta, X. G., Wells, A. R., Kiehart, D. P. and Edwards, G. S.** (2008). Apoptotic force and tissue dynamics during Drosophila embryogenesis. *Science* **321**, 1683-1686.

**Wang, W. and Yoder, J. H.** (2011). Drosophila pupal abdomen immunohistochemistry. *J. Vis. Exp*. **56**, 3139.

**Yamaguchi, Y., Shinotsuka, N., Nonomura, K., Takemoto, K., Kuida, K., Yosida, H. and Miura, M.** (2011). Live imaging of apoptosis in a novel transgenic mouse highlights its role in neural tube closure. *J. Cell Biol.* **195**, 1047-1060.

## Supplemental Information

## Supplemental Figures

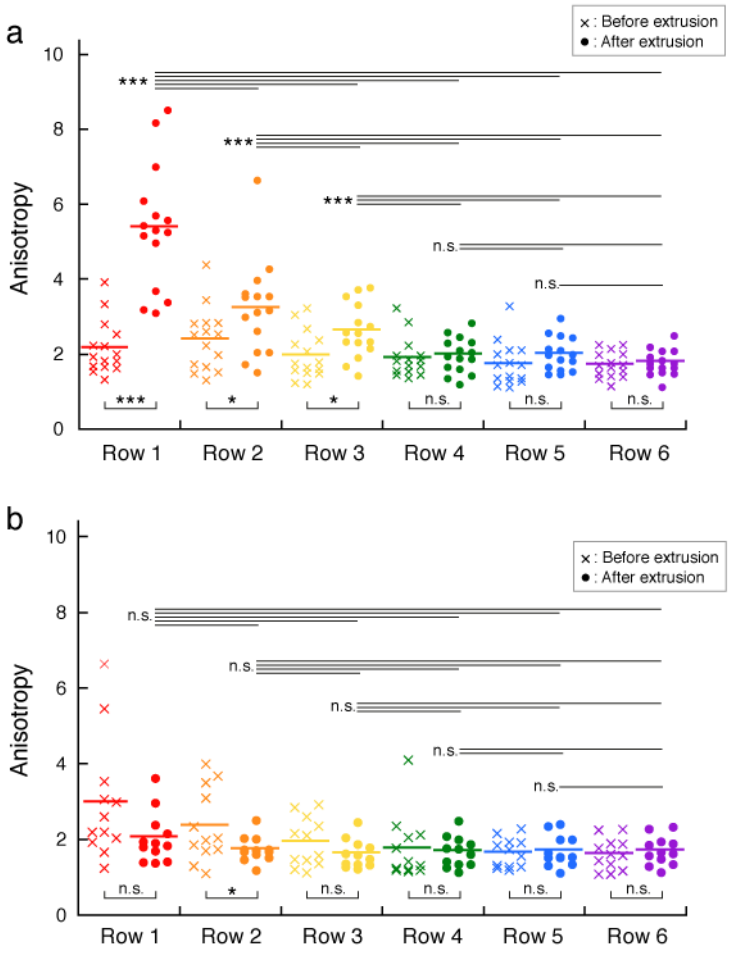


**Fig. S1. Quantification of cell shape deformation of histoblasts upon extrusion of boundary LEC.** (a and b) Plots of anisotropy of cell shape (Supplemental Materials and Methods) before (crosses) and after (filled circles) the boundary cell extrusions, as a function of distance (i.e., number of rows) from the boundary LECs (n=15 from 3 pupae). Data from wild-type pupae (a) and pupa expressing sqh-RNAi only in LECs (b). *: $p<0.05$, ***: $p<0.001$, n.s.: no significance.

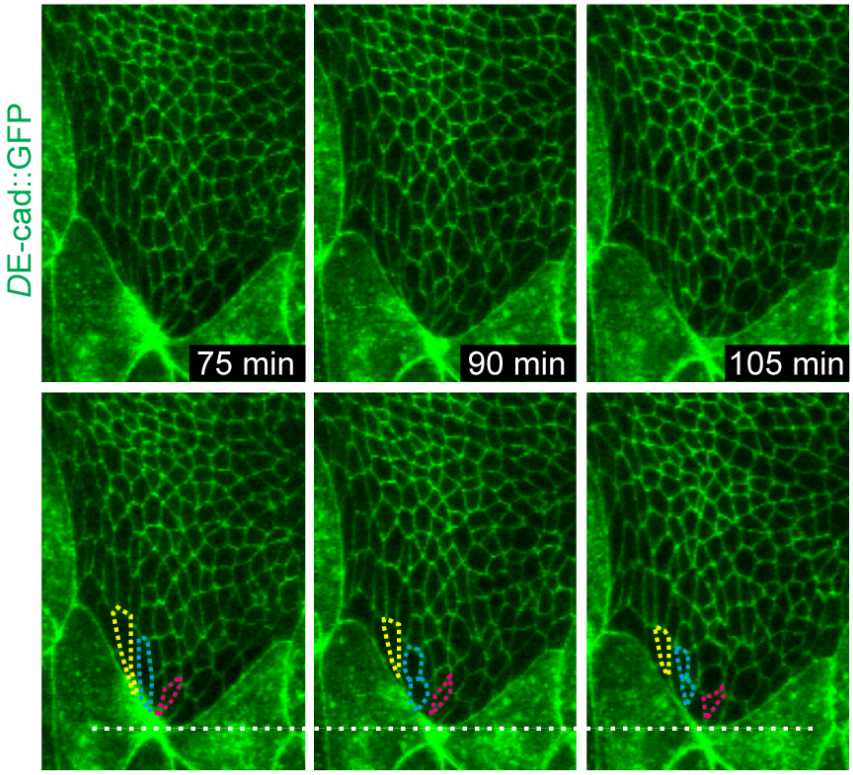


**Fig. S2. Fate of the elongated histoblasts after the completion of apical constriction of apoptotic LEC.** Confocal fluorescence images of wild type pupa expressing *D*E-cad::GFP, showing the fate of the elongated histoblasts presented in Fig. 1 b and 1c. The first time frame (denoted as 75 min) is the same image as the last frame of Fig. 1b (denoted as 75 min). The elongated histoblasts underwent either cell division (highlighted with blue dotted line) or cell-cell junction remodeling (highlighted with yellow and red dotted lines) after the completion of cell extrusion. White dotted line denotes the edge of the histoblasts.

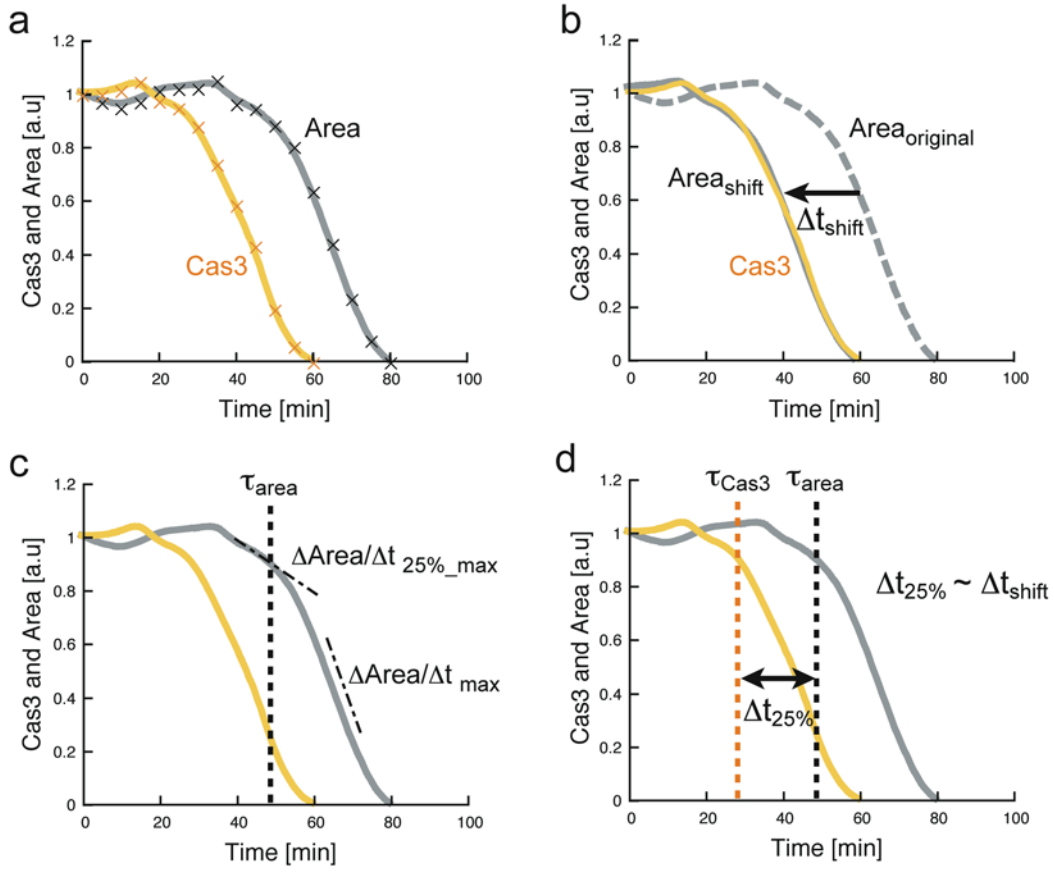


**Fig. S3. Determination of transition time.** Refer to Materials and methods for more detail. (a) Graphs showing the normalized apical area (gray line) and caspase-3 activity (orange) of apoptotic cell over time. (b) Original Area graph ($Area_{original}$, gray dotted line) was shifted by $\Delta t_{shift}$ so that the difference between shifted area ($Area_{shift}$, gray solid line) and caspase-3 data (orange line) is minimized. Note gray and orange solid lines are overlapping each other. (c) Transition time of cell area, $\tau_{area}$ was determined as the time when the derivative of the graph ($\Delta Area/\Delta t$) reached to 25% of the maximum slope ($\Delta Area/\Delta t_{max}$). (d) The time delay between the initiation of apical constriction and caspase-3 activation measured by 25% of maximum slope, $\Delta t_{25\%} = |\tau_{area} - \tau_{Cas3}|$, was consistent to $\Delta t_{shift}$.

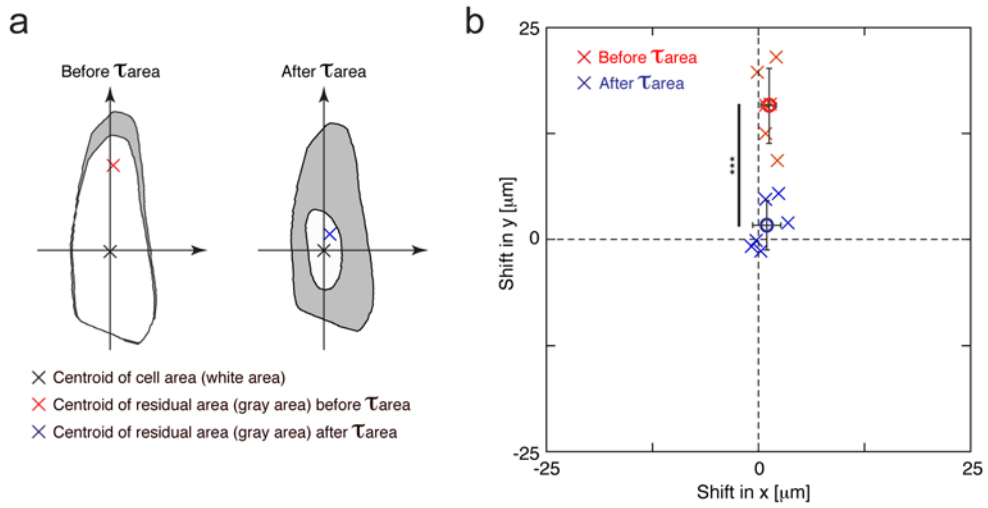


**Fig. S4. Quantitative analyses of the deformation in the shape of extruding LECs.** (a) Two contour plots showing the cell shape of different time points (25 min apart) for before (left) and after (right) $\tau_{area}$. Black cross denotes the centroid of the cell area at later time point (white in the figure). Red and blue crosses denote the centroid of residual area (difrence between two contour plots, gray in the figure) at before and after $\tau_{area}$, respectively. (b) Summary of 6 data. Open circles and error bars represent the average values and the STDEV, respectively. ***: $p<0.001$.

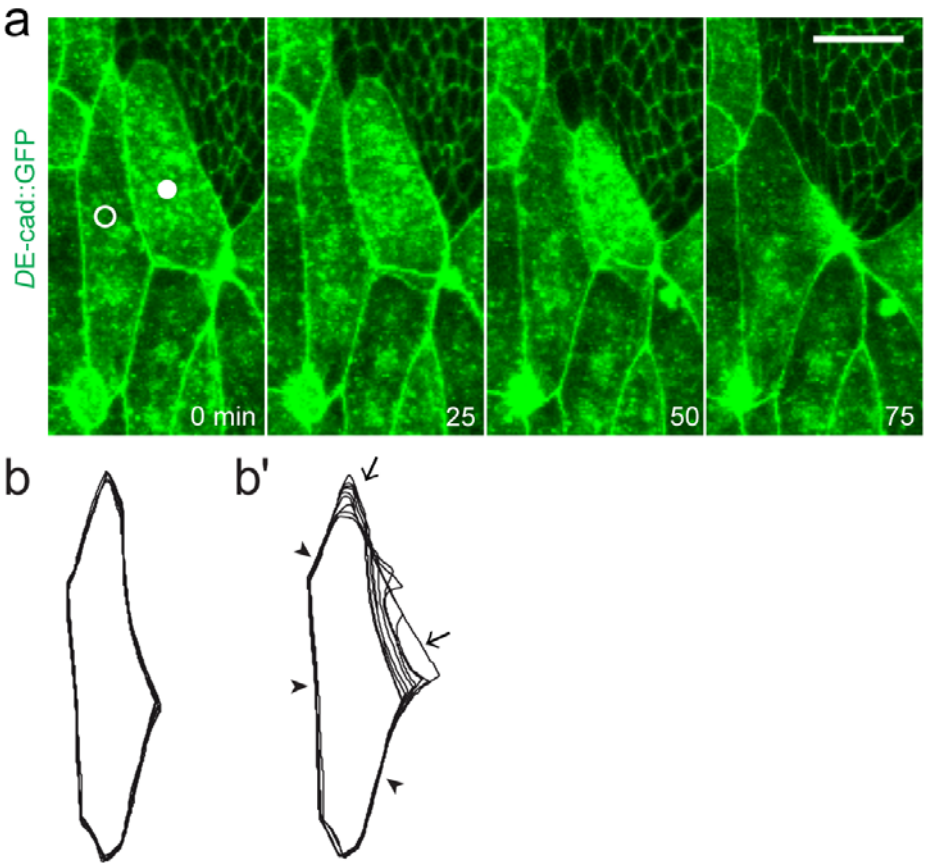


**Fig. S5. Kinematics of a LEC next to an apoptotic LEC.** Confocal fluorescence images of wild type pupa expressing *D*E-cad::GFP, showing the cell shape deformation of a non-dying LEC (highlighted by open circle), which is next to an apoptotic cell (highlighted by filled circle) and same cell as shown in Fig. 1b. Time stamps denote the same time as shown in Fig. 1b. Scale bar, 20 µm. (b) Contour plots showing the cell shape deformation of the non-dying LEC highlighted in (a) prior to $\tau_{area}$ of the apoptotic cell, showing a little deformation. (b') Contour plots of the non-apoptotic LEC from $\tau_{area}$ onwards. The cell deformation is local. Arrow indicates the region with major deformation. Arrowheads highlight the cell boundary with little or no deformation.

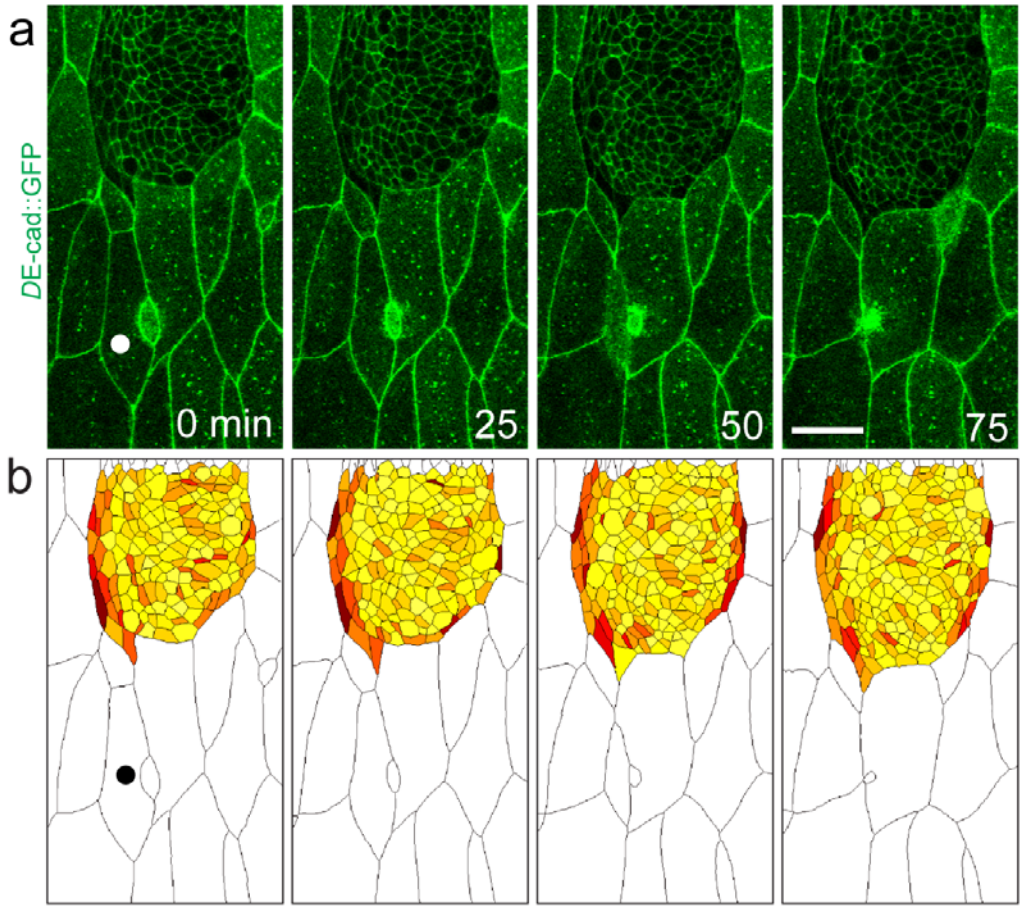


**Fig. S6. Mechanical impact of non-boundary LEC apoptosis.** (a) Confocal fluorescence images of wild type pupa expressing *D*E-cad::GFP. Non-boundary LEC (i.e., one LEC away from histoblast) is highlighted by filled circles. Scale bars, 50 μm. (b) Color-enhanced reproduction of the confocal images from (a). Colors demote the anisotropy of the cell shape: The darker color represent more elongated histoblast cells (same as Fig. 1c). The color of the histoblasts did not change as much as the case of boundary LEC. Scale bar, 20 μm.

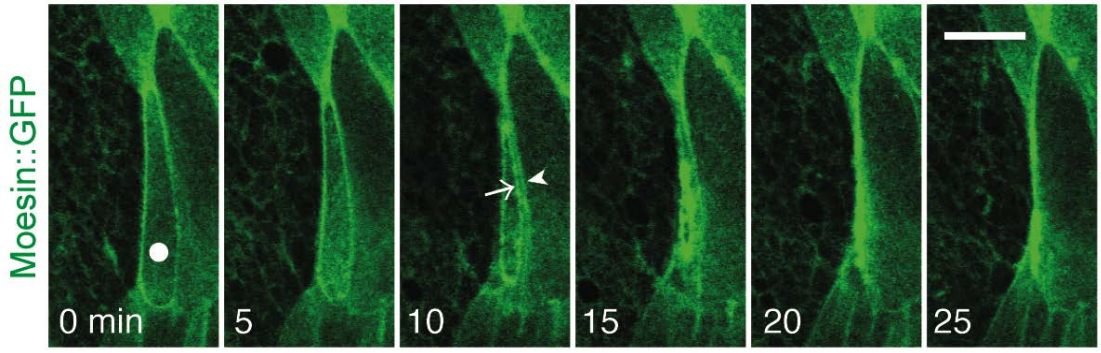


**Fig. S7. Actin distribution around the periphery of apoptotic LEC shows two actin cable-like structures.** Confocal fluorescence images of wild type pupa expressing Moesin::GFP. Apoptotic LECs are highlighted by filled circles. Arrow and arrowhead show the actin accumulation in the apoptotic LEC and the neighboring non-apoptotic LECs, respectively. Scale bar, 20 μm.

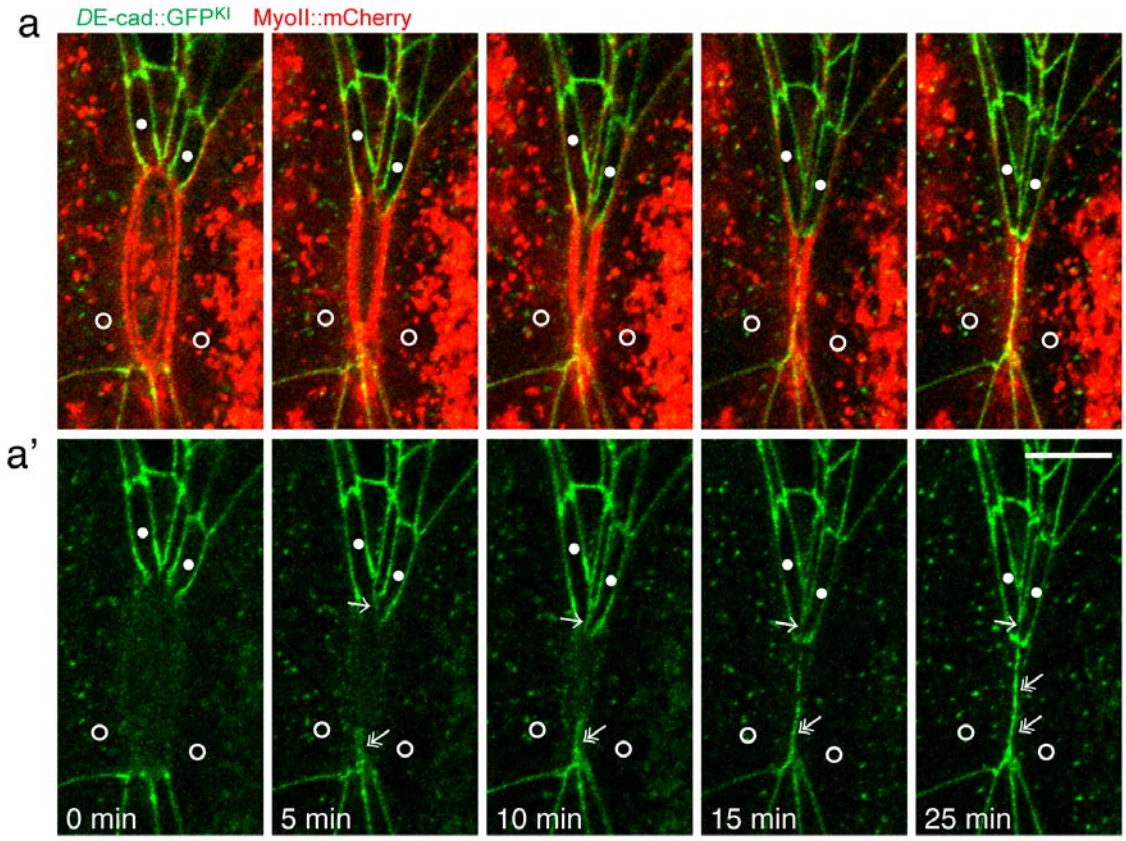


**Fig. S8. Formation of *de novo* AJs between the non-apoptotic neighboring cells.** Confocal fluorescence images of wild type pupae expressing *D*E-cad::GFP and MyoII::mCherry. Two pairs of neighboring cells (filled and open circles) form *de novo* AJs before the completion of apoptotic cell extrusion (arrows and doublearrows). Scale bar, 10 μm.

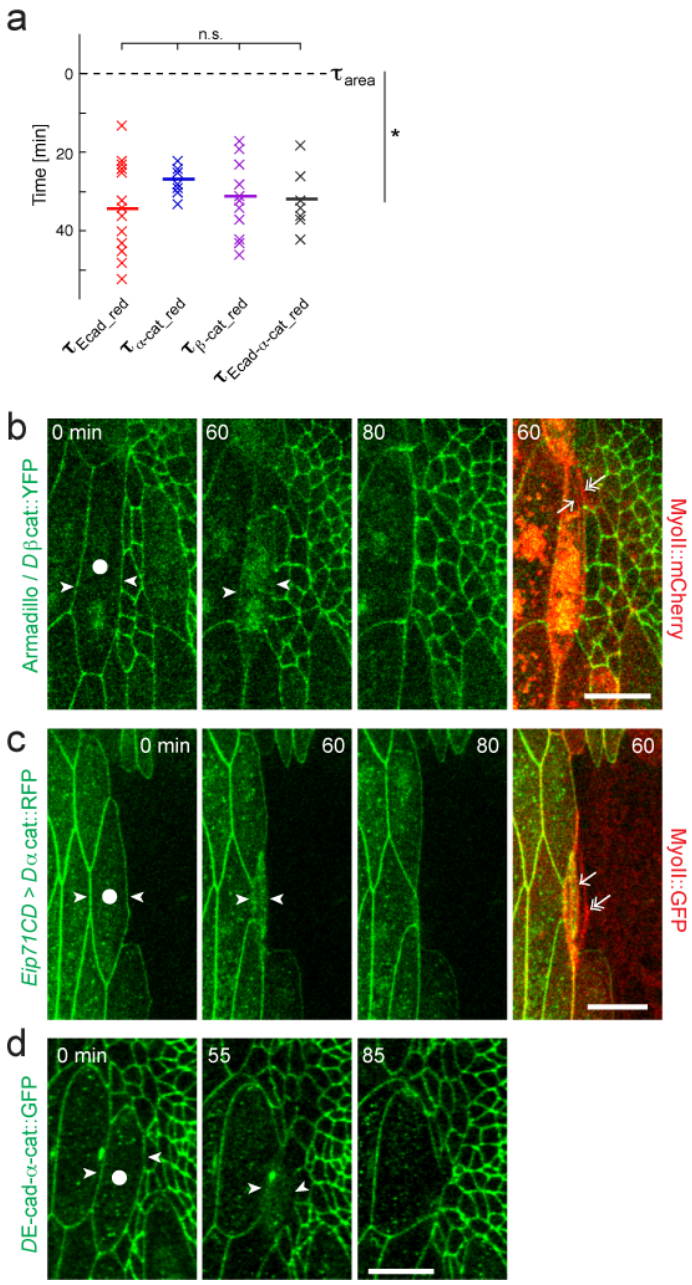


**Fig. S9. Reduction of the level of AJ components during apoptosis.** (a) Time delays of the reduction of AJ components ($\tau_{Ecad\_red}$, $\tau_{\alpha\text{-}cat\_red}$, $\tau_{\beta\text{-}cat\_red}$, and $\tau_{Ecad\text{-}\alpha\text{-}cat\_red}$) using area transition $\tau_{area}$ as a reference (*: $P < 0.05$, n.s.: Not significant). n=13, 9, 12, and 7 for $\tau_{Ecad\_red}$, $\tau_{\alpha\text{-}cat\_red}$, $\tau_{\beta\text{-}cat\_red}$, and $\tau_{Ecad\text{-}\alpha\text{-}cat\_red}$, respectively. Average values are shown as thick horizontal lines. (b and c) Confocal fluorescence images of wild type pupa expressing *D*β-cat::YFP and MyoII::mCherry (b, Movie 7) or pupa expressing α-cat::RFP only in LECs and MyoII::GFP ubiquitously (c, Movie 8). (d) Confocal fluorescence images of pupa expressing GFP tagged fusion protein that the C-terminal domain of E-cad was replaced by an α-cat protein lacking the N-terminal domain (*DE*-cad-α-cat::GFP). Apoptotic LECs are highlighted by filled circles. Arrowheads shows the dissociation of fluorescence signal. Arrows and double arrows denote the myosin in the apoptotic LEC and the neighboring cells, respectively. Scale bars, 20 μm.

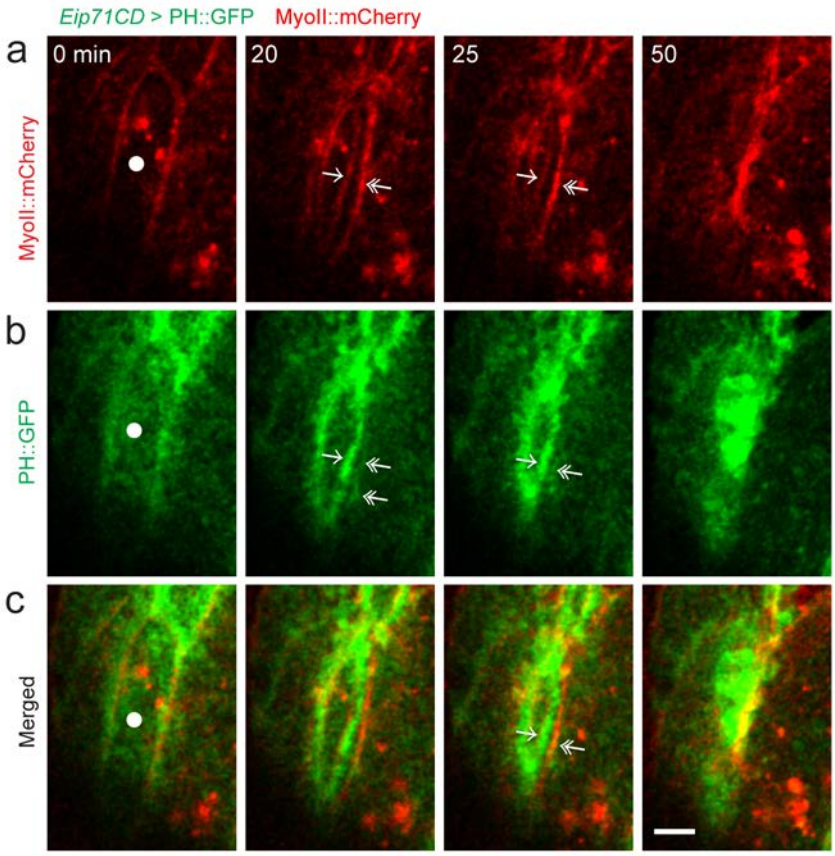


**Fig. S10. AJ disengagement upon apoptosis.** Confocal fluorescence images of wild type pupa expressing the plasma membrane markers PH::GFP in LECs, and MyoII::mCherry ubiquitously, highlighting the plasma membranes of apoptotic (arrow) and neighboring (double arrows) cells detach once the separation of the two myosin cables become apparent. Same data as shown in Fig. 3g. Scale bar, 20 μm.

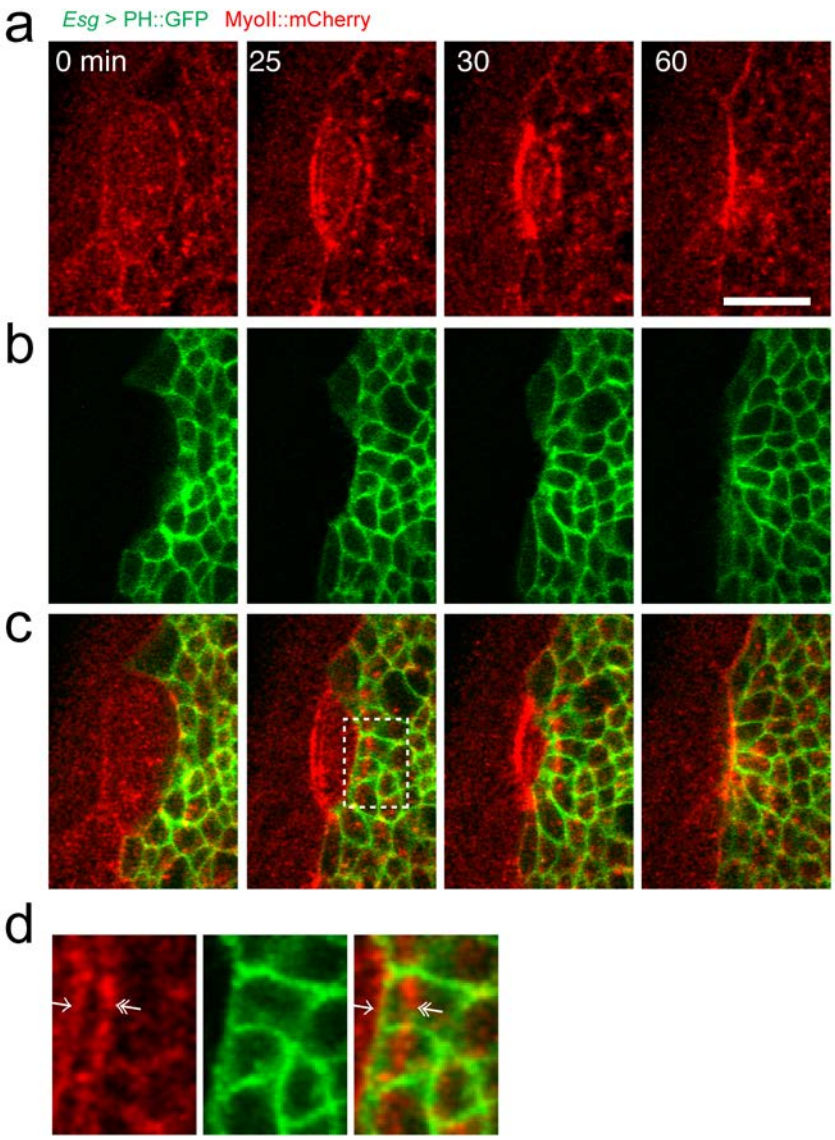


**Fig. S11. AJ non-disengagement upon apoptosis.** (a-c) Confocal fluorescence images of wild type pupa expressing the plasma membrane markers PH::GFP only in the histoblasts, and MyoII::mCherry ubiquitously. (d) High magnification of the dotted region depicted in (c), highlighting the myosin cable in the apoptotic cell (arrow) and the edge of the histoblast membrane are closely juxtaposed each other. Moreover, the myosin cable in the neighboring cells (double arrowheads) is away from the membrane. Scale bar, 20 μm.

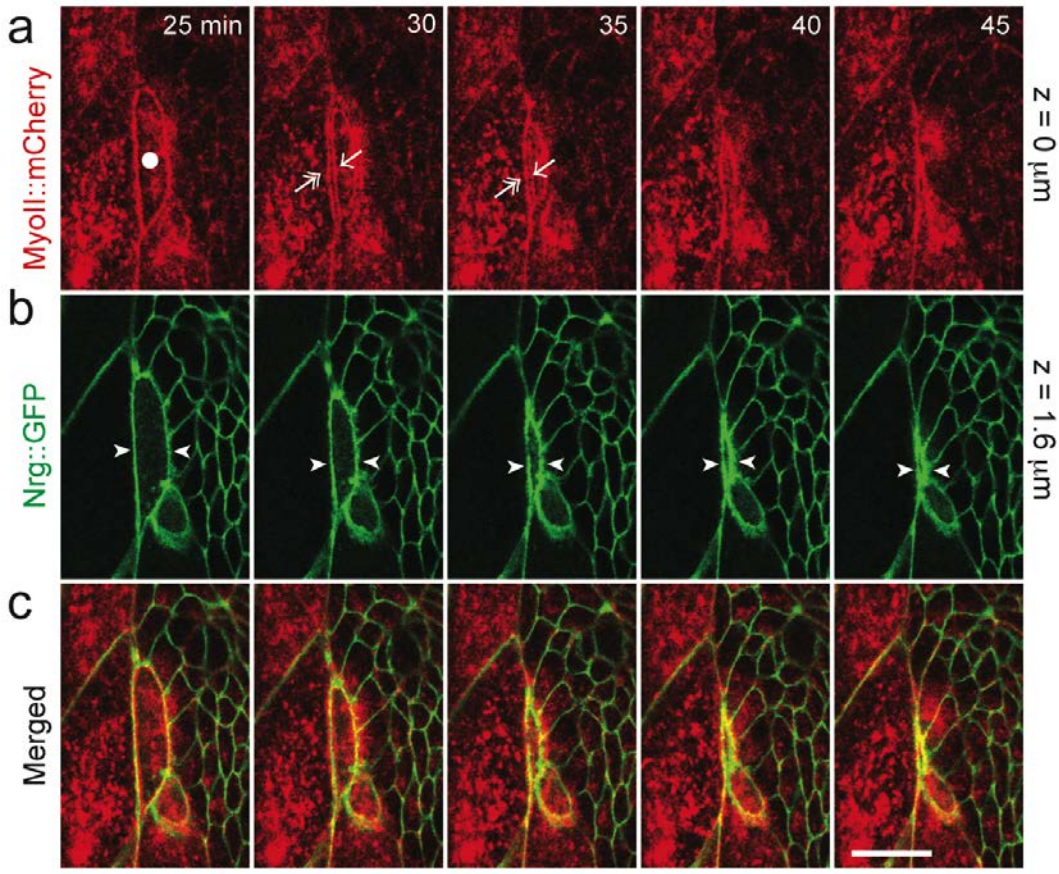


**Fig. S12. Dynamics of septate junction (SJ) during LEC apoptosis.**
(a-c) Confocal fluorescence images of wild type pupa expressing the septate junction marker Nrg::GFP and MyoII::Cherry (Movie 9). Imaging started at 0 min. (a) MyoII images from a z-section at AJ. Apoptotic LEC is highlighted by filled circles. Arrows and double arrows show the MyoII accumulation in the apoptotic LEC and the neighboring LECs, respectively. (b) Images of the septate junction from a z-section 1.6 μm below AJ. Arrowheads indicate the septate junction is not compromised during the apical constriction of the apoptotic cell. (c) Merged image. Scale bar, 20 μm.

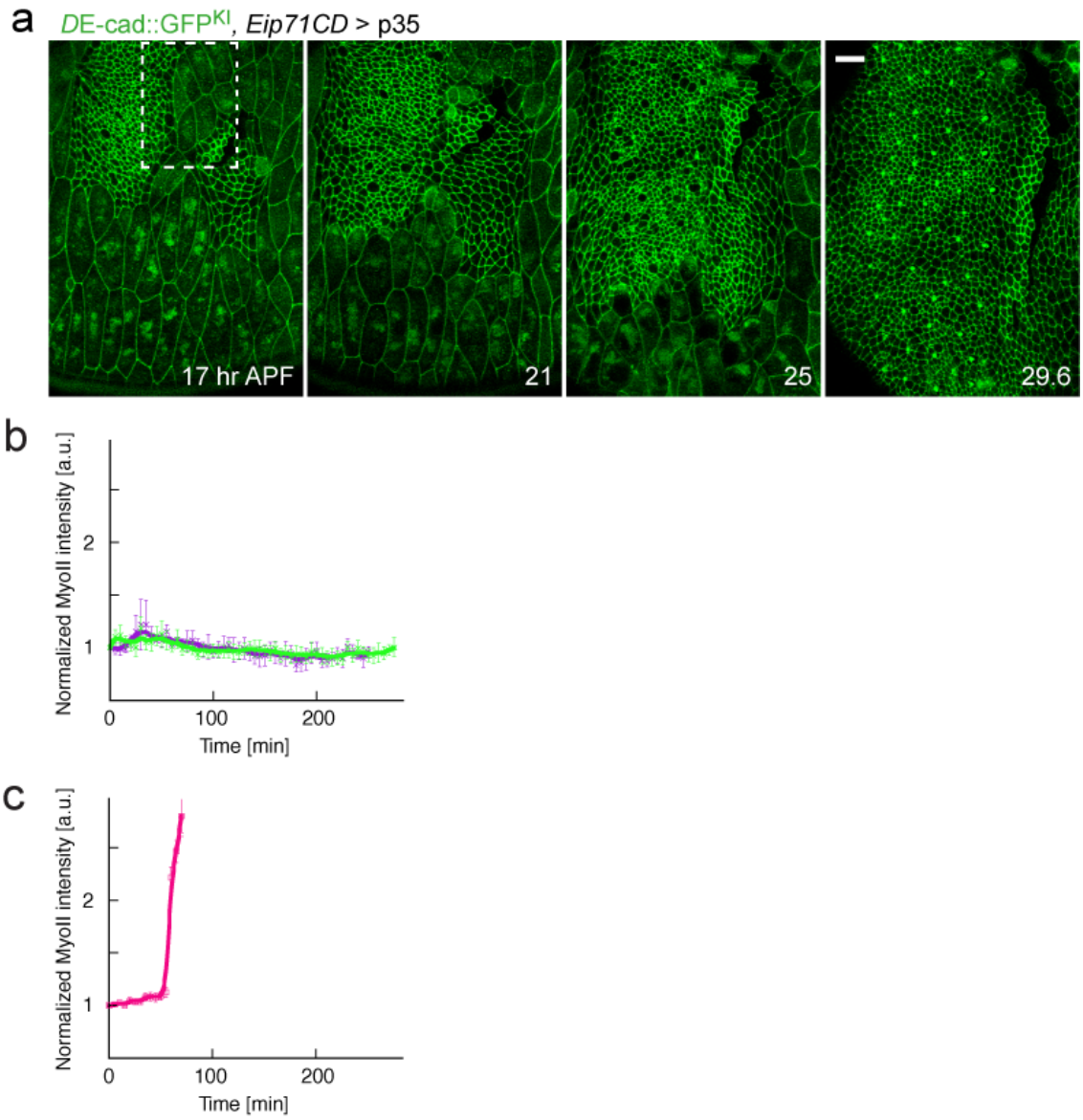


**Fig. S13. Extrusion of LECs expressing caspase inhibitor.** (a) Confocal fluorescence images of pupa expressing caspase inhibitor p35 only in LECs, and *D*E-cad::GFP$^{KI}$ ubiquitously, showing anterior and posterior dorsal histoblast nests and LECs at 17, 21, 25, and 29.6 hours APF. White dotted region represent the field shown in Fig. 5a. Scale bars, 20 μm. (b) Graphs plotting normalized MyoII intensity of extruding cell (green, n=5) and of the summation of extruding cell and neighboring cell (purple, n=7) over time. (c) Graphs plotting normalized MyoII intensity of the summation of apoptotic cell and neighboring cell in wild-type pupae (pink, n=6) over time. Error bars indicate SEM.

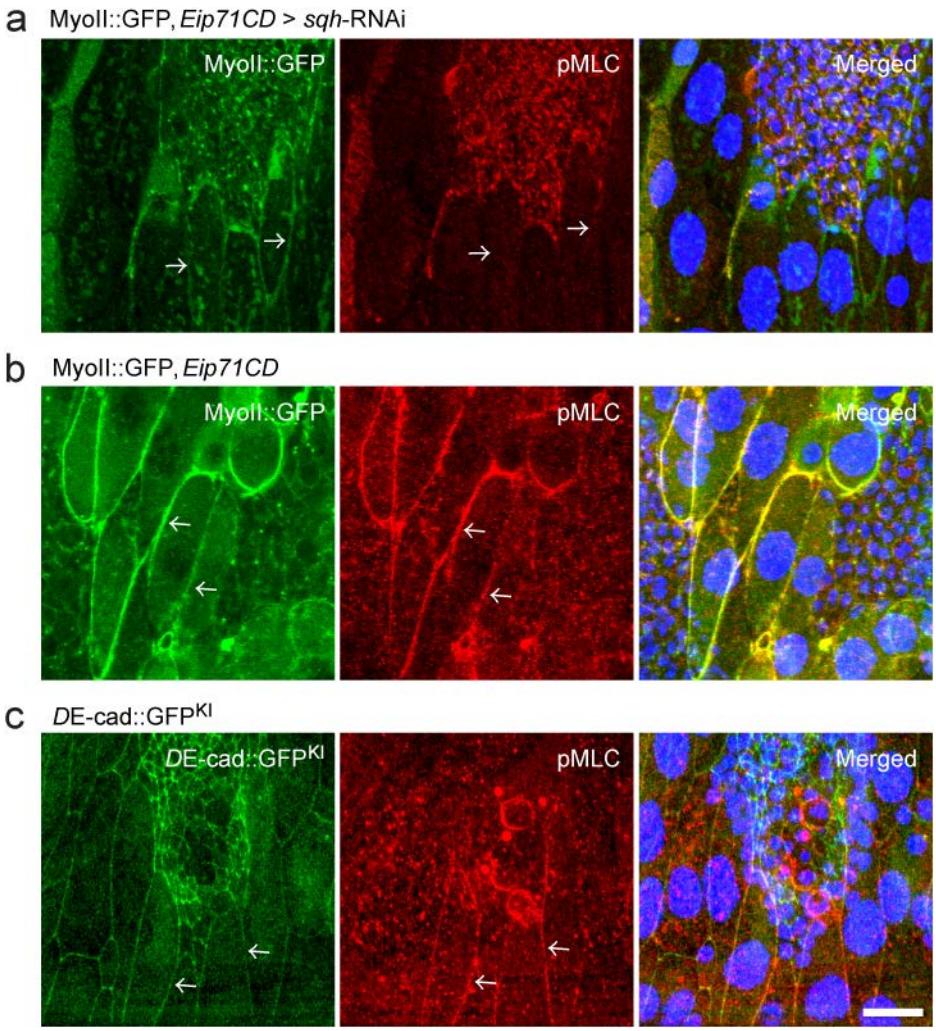


**Fig. S14. Level of phosphorylated myosin regulatory light chain in different pupae.** (a-c) Confocal fluorescence images of pupae stained with phosphorylated myosin regulatory light chain (pMLC, red) and DAPI (blue). (a) Images of pupa expressing sqh-RNAi only in LECs, and MyoII::GFP ubiquitously. (b and c) Images of control pupa expressing MyoII::GFP (b) and *D*E-cad::GFP$^{KI}$ (c), ubiquitously. The level of pMLC at cell boundaries (arrows) in sqh-RNAi expressing LECs is weaker than that of control LECs. Scale bar, 20 µm.

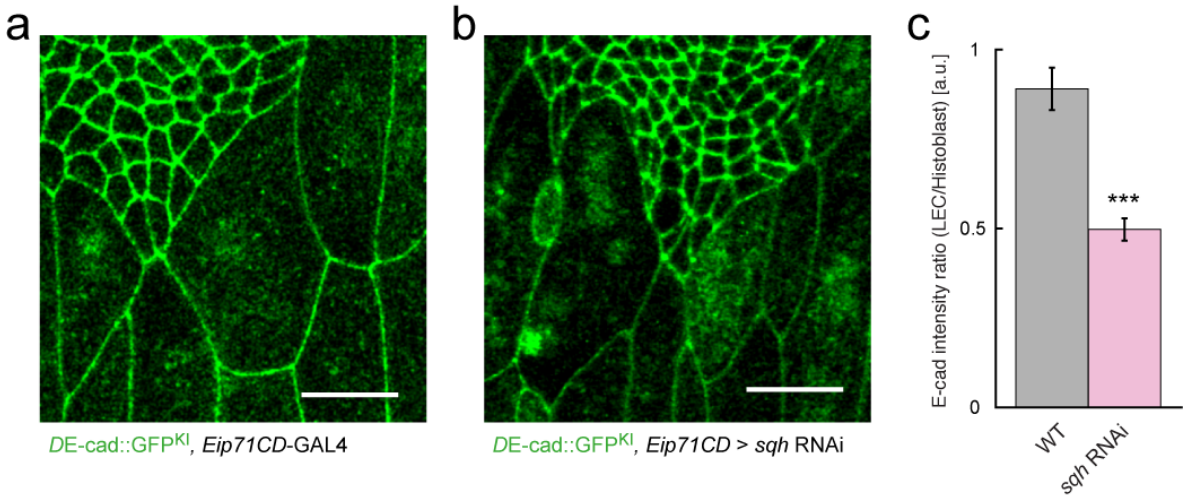


**Fig. S15. Level of E-cad in LECs expressing *sqh*-RNAi.**
(a, b) Confocal fluorescence images of wild-type pupa expressing *D*E-cad::GFP$^{KI}$ ubiquitously (a) or pupa expressing *sqh*-RNAi only in LECs and *D*E-cad::GFP$^{KI}$ ubiquitously (b). The contrast of the images were adjusted so that the fluorescence intensity of histoblasts became equivalent. No apoptotic cells are shown in both images. (c) Statistical comparison of the ratio of E-cad intensity between LEC and histoblast. Gray and light red bars denote the mean values from wild-type and sqh-RNAi expressing LECs, respectively (n=5 and 8). Each ratio was calculated based on the average of 20 cell boundaries of LECs and histoblast from an image. Scale bars, 20 μm

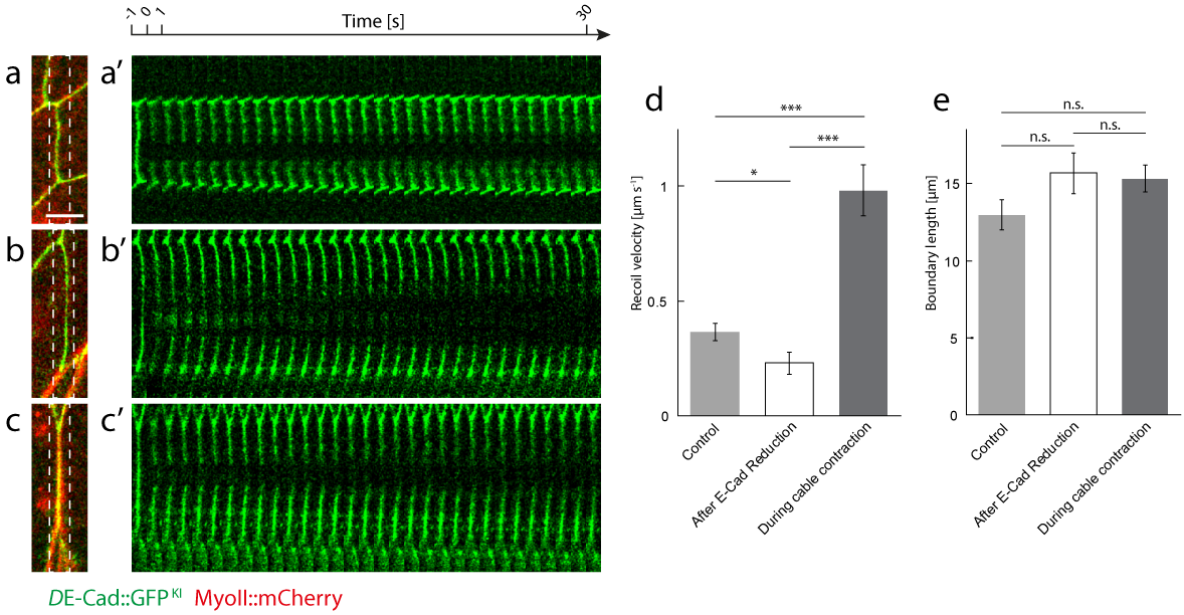


**Fig. S16. Tissue tension release and reshape after reduction of E-cad levels in LECs.** (a-c) Confocal fluorescence images of wild-type pupa expressing *D*E-cad::GFP$^{KI}$ and MyoII::mCherry ubiquitously highlighting the LEC boundaries connected to the apoptotic LEC before ablation. (a'-c') Kymographs generated from the white boxed regions in a-c, showing the dynamics of the cell boundaries after ablation. The ablations were performed in three different stages of apoptotic cell extrusion: before reduction of E-cad levels (a and a'); right after reduction (b and b'); and during neighboring actomyosin cable (double-arrow in c) contraction (c and c'). Scale bar, 10 μm. Statistical comparison of the recoil velocities (d) and the length of cell boundary at laser ablation (e) at each stage of cell extrusion shown in a-c. n=16, 11 and 13 for control, after reduction, and, during cable contraction, respectively. Error bars indicate SEM. *: $P < 0.05$, ***: $P < 0.001$, n.s.: no significance.

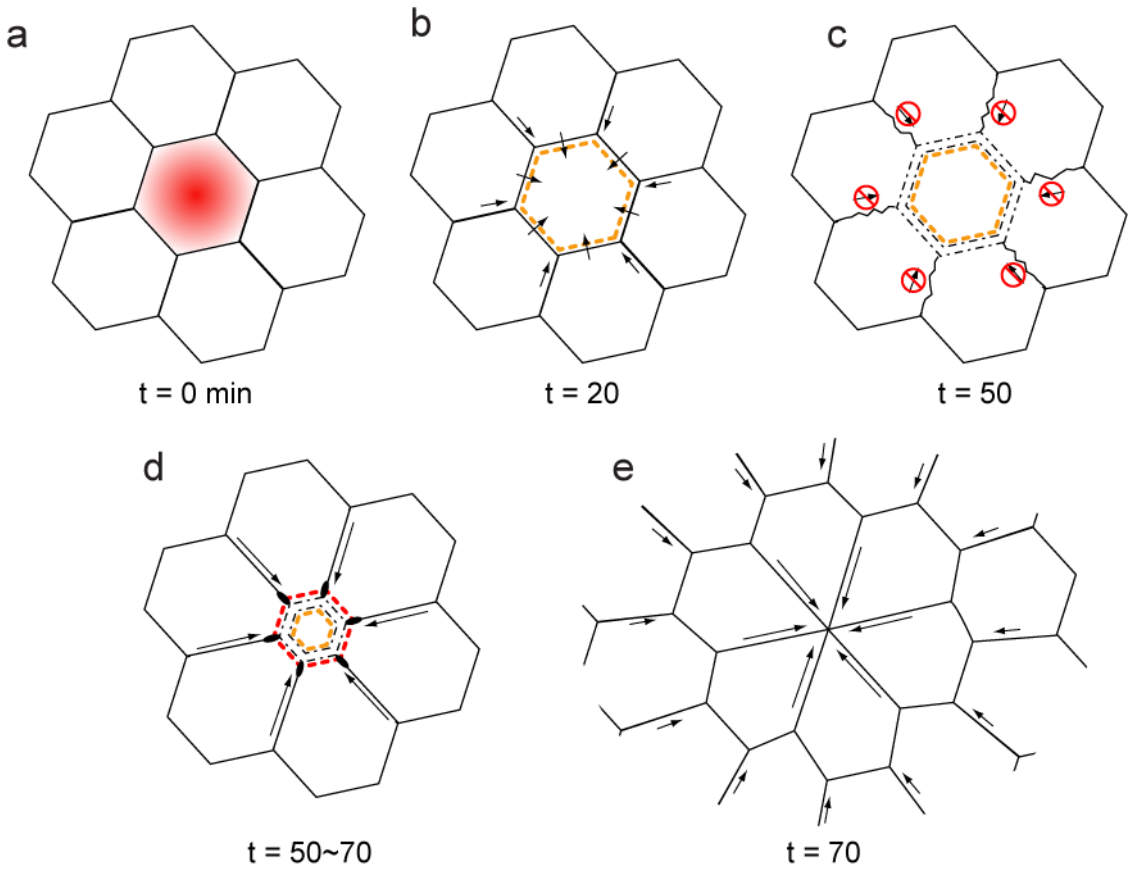


**Fig. S17. A model of the progressive remodeling of AJ and tissue tension during apoptosis.** Cartoons show the progression of apoptotic events with the top view at the AJ. Cell size and shape are not scale. (a) Caspase activation (set this time as t=0min). (b) Beginning of apical constriction and MyoII accumulation (orange dotted line) in the apoptotic cell (t=20min). The contraction of the actomyosin cable pulls the neighboring cells through the AJ (black arrows). (c) AJ disengagement (black dotted lines) and tension release (t=50min). (d) MyoII accumulation in neighboring non-apoptotic cells (red dotted lines). Contraction of supra-cellular actomyosin cables reshape the tissue tension (black arrows) (t=50-70min). (e) End of apical constriction. The propagation of mechanical force promotes tissue dynamics (black arrows) (t=70min).

## Supplementary Materials and Methods

### *Drosophila* stocks and Genetics

Otherwise stated, fly stocks were obtained from the Bloomington Stock Center. The following lines were used: *ubi*-E-cad::GFP (H. Oda), Nrg::GFP (Kyoto Stock Center), moe::GFP (D. Kiehart), *ubi*-E-cad::GFP; *sqh*-*Sqh*-mCherry (A.C. Martin), Armadillo::YFP , and Knock-in alleles of *D*E-cad::GFP and *D*E-cad::mTomato (Huang et al., 2009). The following UAS and GAL4 were used to ectopically express the gene of interest: UAS-*sqh*::GFP (M. Affolter), UAS-α-catenin::RFP (K. Sugimura), UAS-*sqh*-RNAi (VDRC), UAS-SCAT3 (M. Miura), UAS-p35, *Esg*-GAL4, *Eip71CD*-GAL4, and *tsh*-GAL4. Live imaging of E-cad and caspase-3 sensor SCAT3 was carried out by crossing *tsh*-GAL4, UAS-SCAT3/CyO (M. Miura) with *D*E-cad::mTomato (Huang et al., 2009).
*sqh*-RNAi MARCM clones that were positively marked by the double copy of histone-RFP expression were recovered from neoFRT19A, *tubP*-Gal80, *hs*FLP; UAS-*sqh*-RNAi (male), and neoFRT19A, *ubi*-mRFP.nls; *ubi*-E-cad::GFP, *Eip71CD*-GAL4 (female). Mitotic clones were induced using the FLP-FRT technique by using the *hs*-FLP with heat shock for 50 min at 37°C in early embryos. The genotypes of three cells analyzed in Fig. 7b are, neoFRT19A, tubP-Gal80, hsFLP/neoFRT19A, ubi-mRFP.nls; UAS-sqh-RNAi/ DE-cad::GFP-KI, Eip71CD-GAL4; +/+ ($LEC_{WT/WT}$), neoFRT19A, tubP-Gal80, hsFLP/neoFRT19A, tubP-Gal80, hsFLP; UAS-sqh-RNAi/ DE-cad::GFP-KI, Eip71CD-GAL4; +/+ ($LEC_{WT/RNAi}$), and neoFRT19A, ubi-mRFP.nls/neoFRT19A, ubi-mRFP.nls; UAS-sqh-RNAi/ DE-cad::GFP-KI, Eip71CD-GAL4; +/+ ($LEC_{RNAi}$).

### Cell shape anisotropy analysis

To measure the anisotropy of individual histoblast cell (Fig. 1c and Fig. S1), the z-projected E-cad::GFP time-lapse images were first segmented by Packing Analyzer V2.0 (Aigouy et al., 2010). The cell boundary data were subsequently analyzed with Matlab software (MathWorks, MA, USA). Segmented cell shapes were fitted by ellipse, which was optimized by maximizing the area overlap between a segmented cell shape and an ellipse. Anisotropy of the cell was defined as the ratio of minor and major axes of the fitting ellipse.

### Caspase-3 activity analysis

To monitor caspase-3 activity (Fig. 2a and Movie 5), fly with FRET base caspase-3 sensor, SCAT3 (Nakajima et al., 2011, Takemoto et al., 2003) was used. A 405nm laser was used to excite ECFP and two fluorescence images (ECFP and Venus) were simultaneously captured. FRET ratio was calculated by taking the intensity ratio between the sum-intensity z-projected ECFP and Venus images. FRET ratio of an apoptotic LEC (Fig. 2c) was measured by averaging the FRET ratio within an apoptotic cell. The shape of an apoptotic cell was manually segmented from the sum-intensity z-projected Venus images over time by using ImageJ (Schneider et al., 2012).

### Determination of the transition time

To measure the time delay between the beginning of apical constriction and caspase-3 activation (Fig. 2c), we first normalized the cell area and caspase-3 activity data to the value measured at time = 0 sec (Fig. S3a). The area data was shifted in time to minimize the difference between area and caspase-3 data (Fig. S3b). The shift was defined as $\Delta t_{shift}$.

To determine when the cell started to constrict with higher speed ($\tau_{area}$) and when the cell started to activate its Cas-3 activity ($\tau_{Cas3}$) without comparing the two graphs, we referred to the maximum derivative of each graphs. We defined $\tau_{area}$ as the time when the derivative of the graph reached to 25% of the maximum slope (Fig. S3c). Similarly, we defined $\tau_{Cas3}$. The time delay between the initiation of apical constriction and caspase-3 activation measured by 25% of maximum slope, $\Delta t_{25\%} = |\tau_{area} - \tau_{Cas3}|$, was consistent to $\Delta t_{shift}$ (Fig. S3d). With the other values, e.g., numbers between 10% and 40%, $|\tau_{area} - \tau_{Cas3}|$ was not as close to $\Delta t_{shift}$ as 25%.

Same setting (25% of the maximum slope) was used to define the transition time not only for $\tau_{area}$ and $\tau_{Cas3}$, but also for all the other data, for instance $\tau_{EcadKI}$, $\tau_{outer\_MyoII}$ and $\tau_{inner\_MyoII}$.

**MyoII intensity analysis**

To quantify the progression of MyoII accumulation in apoptotic LECs or neighboring cells, the average fluorescent intensity of MyoII::GFP signal either from histoblast that originally attached to apoptotic LEC (Fig. 4a') or solely originated from the cell periphery of apoptotic LECs (Fig. 4c') were measured. Images of sum-intensity z-projection (around AJ) of MyoII::GFP were analyzed over time. ROIs (see main text for more detail) to calculate the intensity were manually defined by the free-hand line tools of ImageJ. The total intensity along the line with thickness of 4 pixels (0.24 μm/pixel) was measured and divided by the length of the line.

**Cell boundary linearity measurement**

Linearity of the histoblast cell boundaries was calculated as a ratio of the two ends of boundary (measured by using ImageJ Straight Line tool) to the actual length of the histoblast cell boundary (measured by using ImageJ Segmented Line tool). A linearity value 1 represents a straight line.

**Calculation of initial recoil velocity after ablation**

The length of ablated cell boundary was measured overtime by using ImageJ Straight Line tool. Data points before the cut were fit with linear line. An exponential was used to fit the data after the cut. The effective time of the cut was found as the intersection of the linear line with the exponential. The initial recoil velocity was found from the deliberative of the exponential at effective time of the cut. The velocity was calculated in Matlab. More detail can be found in (Hara et al., 2016).

**Quantitative analyses of the deformation in the shape of extruding LECs**

To quantify the local/isotropic deformation of extruding LEC, as shown in Fig. 1e (before $\tau_{area}$) and 1e' (after $\tau_{area}$), we first measured the differences in cell shapes at two different time points (Fig. S4a). Before $\tau_{area}$, the differences in cell shapes at [$\tau_{area}$-25] min and $\tau_{area}$ min was shown as gray area in Fig. S4a (left). The centoid of this gray area (residual area) and the cell area at $\tau_{area}$ (white area) were shown as a red and black cross, respectively. We then defined the black cross as the origin of the new coordinate system. We further rotated the coordinate so that y-axis represented the direction toward histoblast. After $\tau_{area}$, the differences in cell shapes at $\tau_{area}$ min and [$\tau_{area}$+25] min was shown as gray area in Fig. S4a (right). The centoid of this gray area (residual area) and the cell area at [$\tau_{area}$+25] (white area) were shown as a blue and black cross, respectively. Finally, we analyzed 6 cells before and after $\tau_{area}$, and summarized all data in a same graph (Fig. S4b).

## Supplemental References

Aigouy, B., Farhadifar, R., Staple, D.B., Sagner, A., Roper, J.C., Julicher, F. & Eaton, S. (2010). Cell flow reorients the axis of planar polarity in the wing epithelium of Drosophila. *Cell,* 142**,** 773-86.

Hara, Y., Shagirov, M. & Toyama, Y. (2016). Cell Boundary Elongation by Non-autonomous Contractility in Cell Oscillation. *Current biology : CB,* 26**,** 2388-96.

Huang, J., Zhou, W., Dong, W., Watson, A.M. & Hong, Y. (2009). Directed, efficient, and versatile modifications of the Drosophila genome by genomic engineering. *Proceedings of the National Academy of Sciences,* 106**,** 8284-8289.

Nakajima, Y.-I., Kuranaga, E., Sugimura, K., Miyawaki, A. & Miura, M. (2011). Nonautonomous Apoptosis Is Triggered by Local Cell Cycle Progression during Epithelial Replacement in Drosophila. *Molecular and Cellular Biology,* 31**,** 2499-2512.

Schneider, C.A., Rasband, W.S. & Eliceiri, K.W. (2012). NIH Image to ImageJ: 25 years of image analysis. *Nature methods,* 9**,** 671-5.

Takemoto, K., Nagai, T., Miyawaki, A. & Miura, M. (2003). Spatio-temporal activation of caspase revealed by indicator that is insensitive to environmental effects. *The Journal of cell biology,* 160**,** 235-43.

## Supplemental Movies

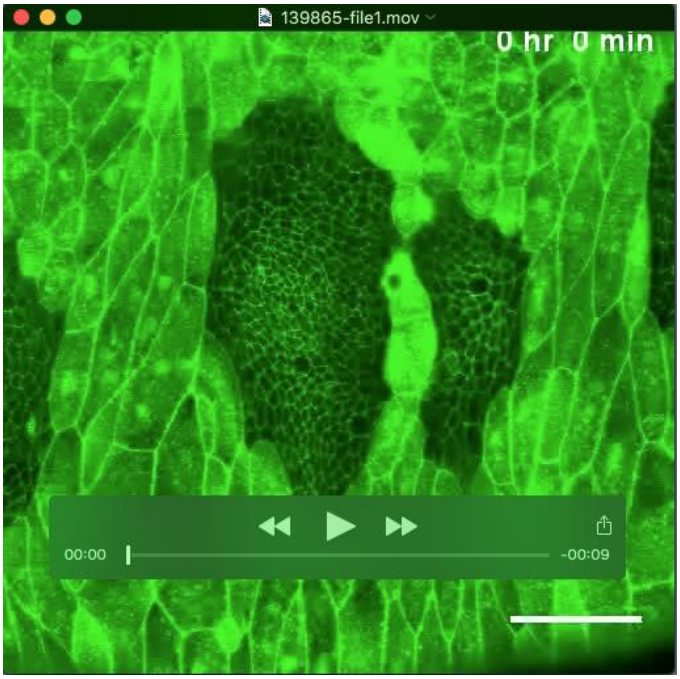


**Movie 1.** Time-lapse images of wild-type pupa expressing *ubi-D*E-cad::GFP. Scale bar, 50 µm.

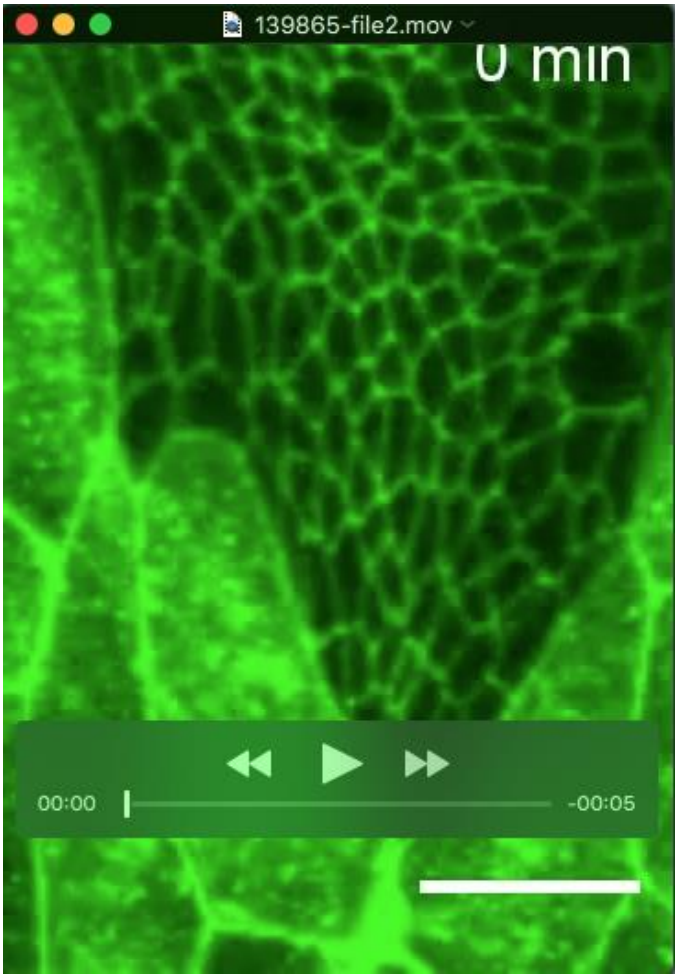


**Movie 2.** Time-lapse images of wild-type pupa expressing *ubi-D*E-cad::GFP. Scale bar, 20 μm.


**Movie 3.** Time-lapse images of wild-type pupa expressing Lifeact::GFP. Top view and orthogonal views. Scale bar, 20 µm.

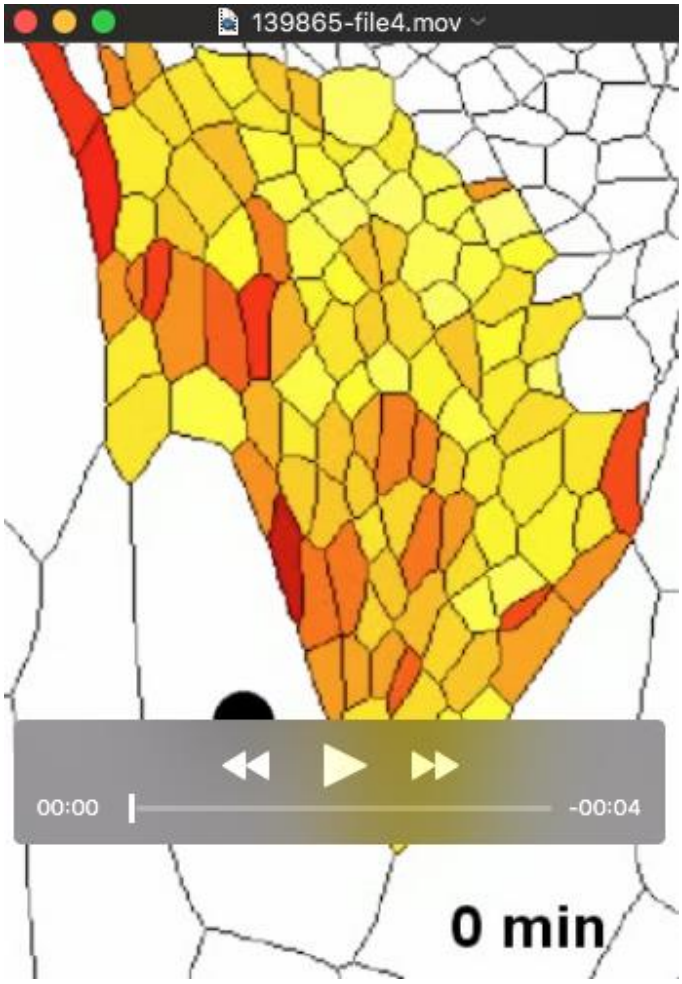


**Movie 4.** Color-enhanced reproduction of the confocal images from Movie 3. Colors demote the anisotropy of cell shape (as illustrated by the color bar in Fig. 1c).

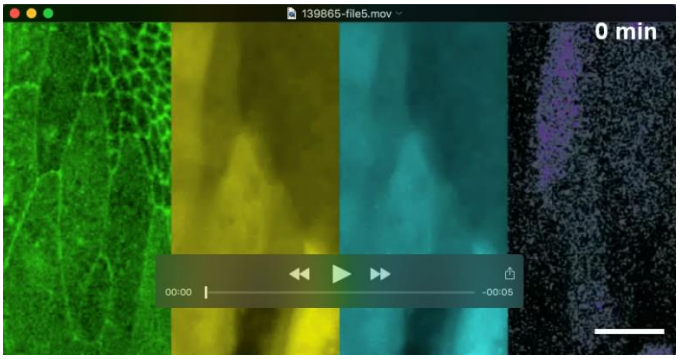


**Movie 5.** Time-lapse images of wild-type pupa expressing *D*E-cad::mTomato$^{KI}$ (green), FRET-base caspase-3 sensor SCAT3 (Venus: yellow, ECFP: cyan), and FRET ratio (perple - white). Scale bar, 20 μm.

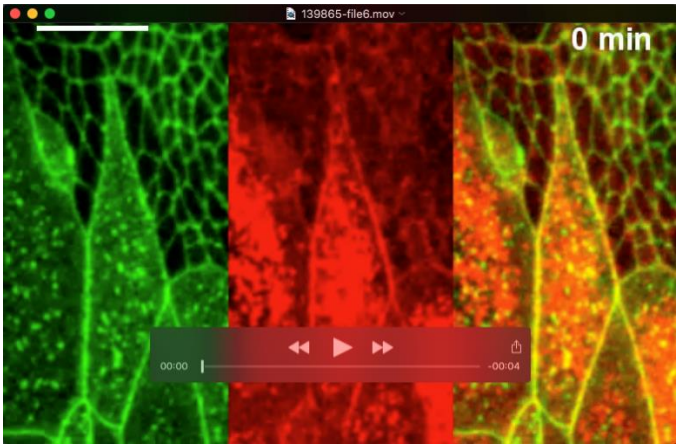


**Movie 6.** Time-lapse images of of wild-type pupa expressing *ubi-D*E-cad::GFP (green) and MyoII::Cherry (red). Scale bar, 20 μm.

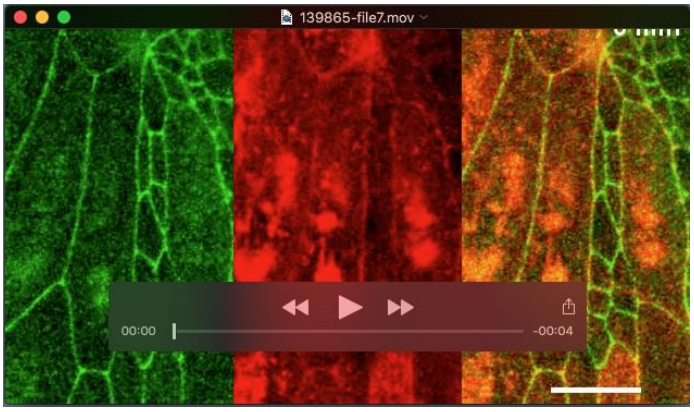


**Movie 7.** Time-lapse images of wild-type pupa expressing β-cat::YFP (green) and MyoII::Cherry (red). Scale bar, 20 μm.

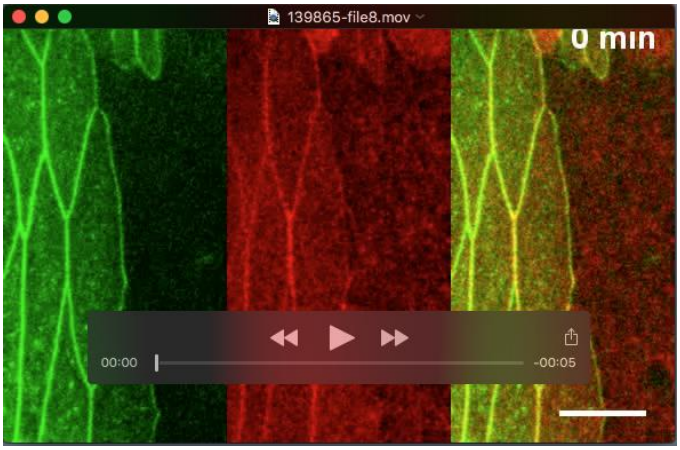


**Movie 8.** Time-lapse images of wild-type pupa expressing α-cat::RFP (green) and MyoII::GFP (red). Scale bar, 20 μm.

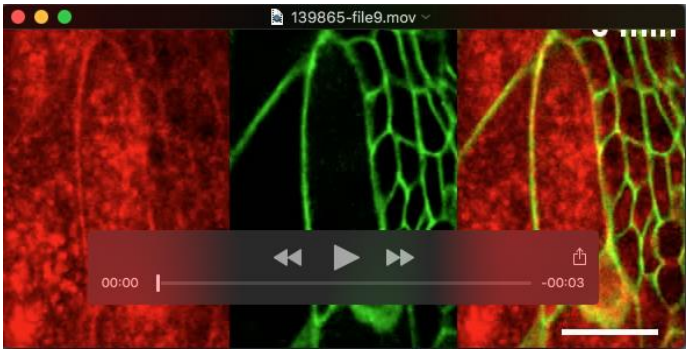


**Movie 9.** Time-lapse images of wild-type pupa expressing Nrg::GFP (green) and MyoII::Cherry (red). Scale bars, 20 μm.

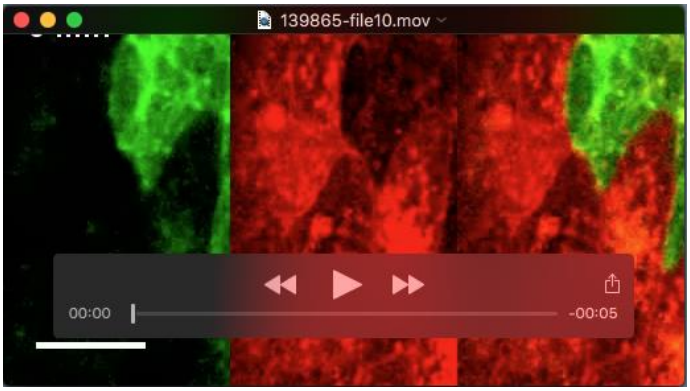


**Movie 10.** Time-lapse images of wild-type pupa expressing MyoII::GFP in histoblasts (green) and MyoII::Cherry (red) ubiquitously. Scale bar, 20 μm.

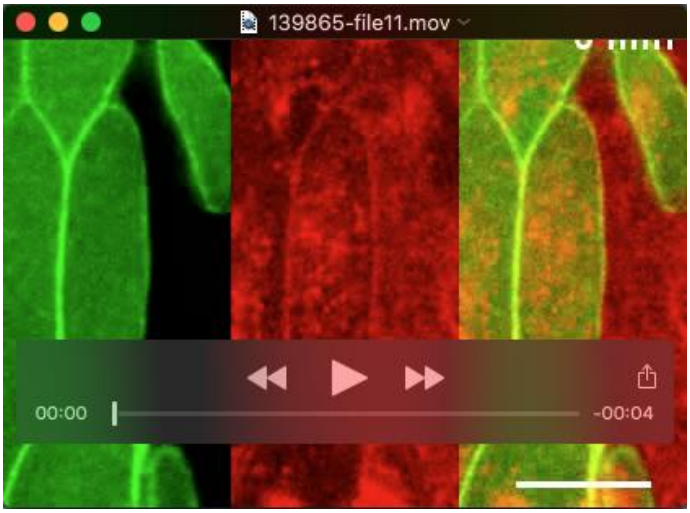


**Movie 11.** Time-lapse images of wild-type pupa expressing MyoII::GFP in LECs (green) and MyoII::Cherry (red) ubiquitously. Scale bar, 20 µm.

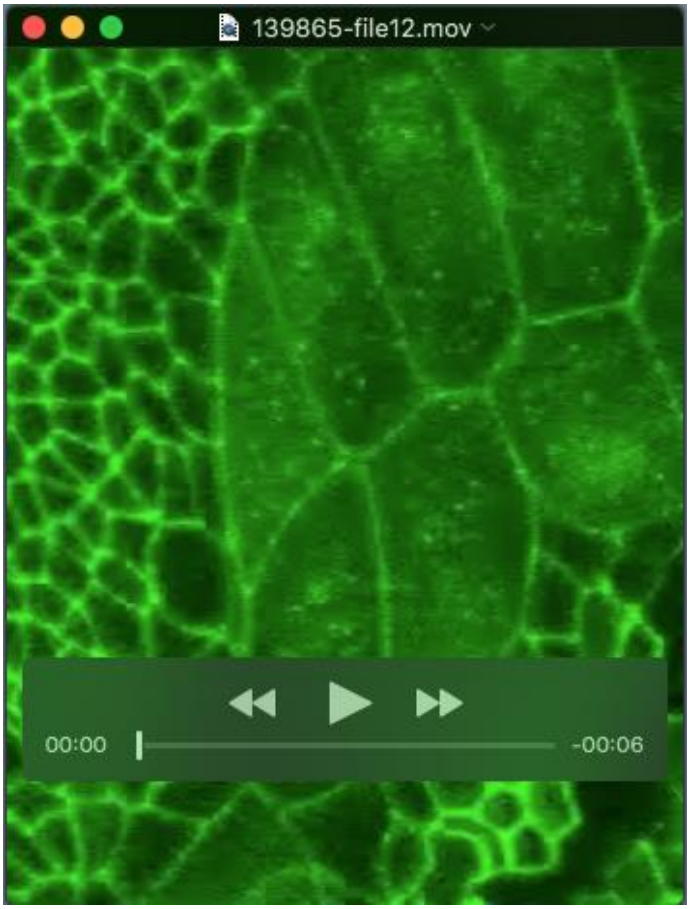


**Movie 12.** Time-lapse images of pupa expressing caspase inhibitor p35 only in LECs and expressing E-cad::GFP$^{KI}$ (green) ubiquitously. Scale bar, 20 µm.

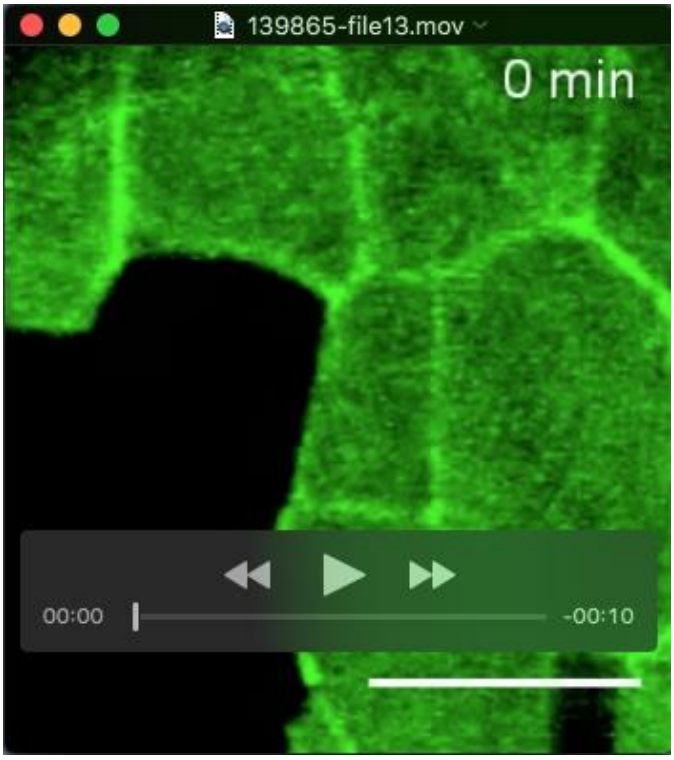


**Movie 13.** Time-lapse images of pupa expressing caspase inhibitor p35 and MyoII::GFP (green) only in LECs. Scale bar, 20 μm.

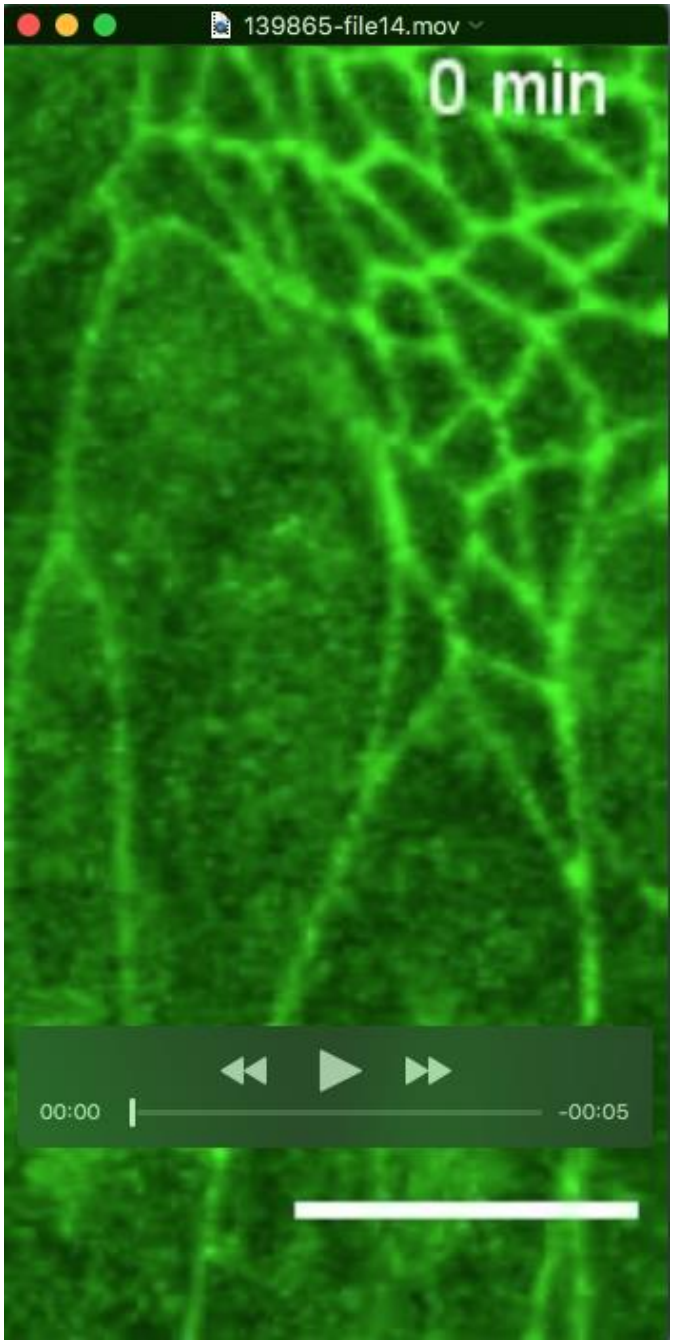


**Movie 14.** Time-lapse images of pupa expressing sqh-RNAi only in LECs and expressing E-cad::GFP$^{KI}$ (green) ubiquitously. Scale bar, 20 μm.

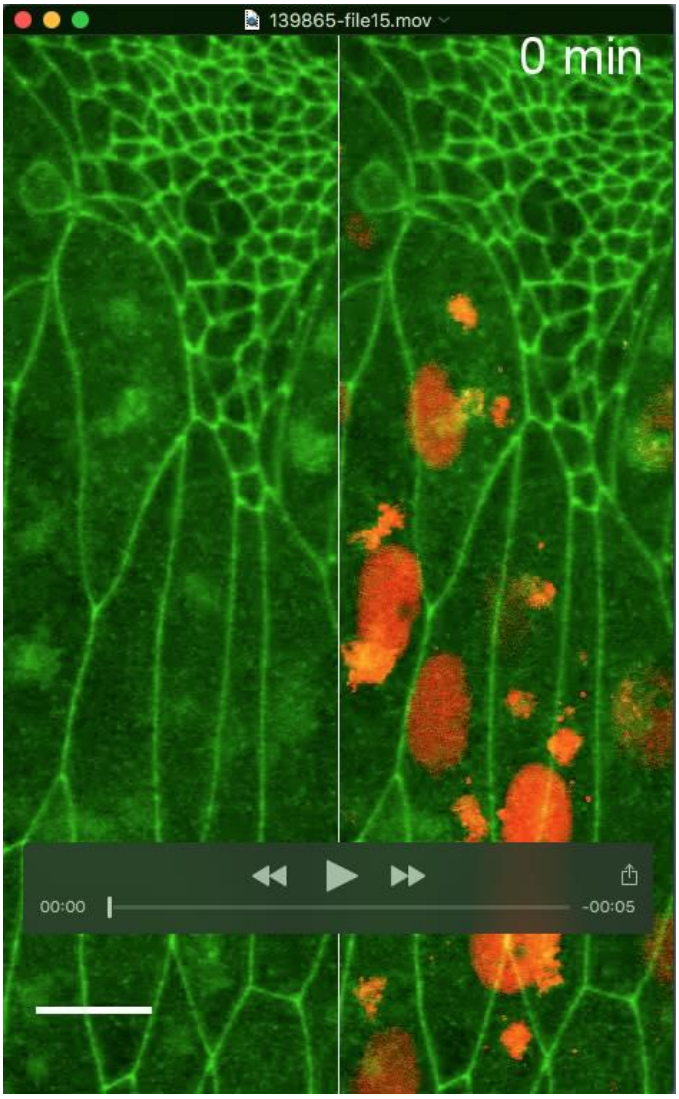


**Movie 15.** Time-lapse images of pupa with clonal expression of *sqh*-RNAi. E-cadherin::GFP (green) and Histone::Cherry (red). Scale bar, 20 μm.

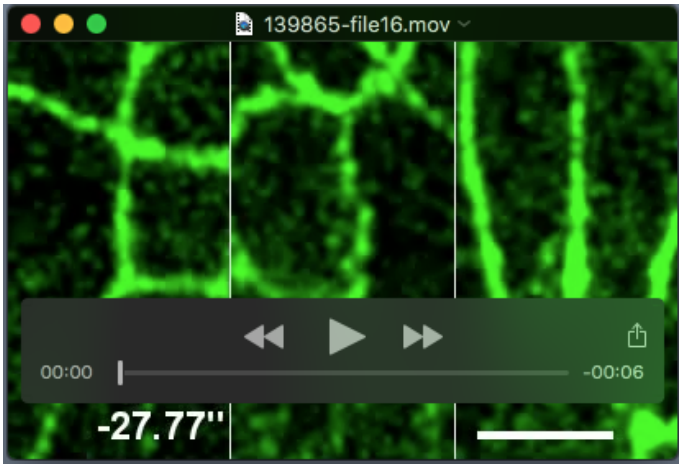


**Movie 16.** Time-lapse images of laser ablation on pupa with *D*E-cad::GFP. The ablations were performed in three different stage of apoptotic cell extrusion: before the reduction of E-cad (left); right after the reduction of E-cad (middle); and during the contraction of actomyosin cable in the neighboring cells (right). Scale bar, 5 μm.